The Spin–orbit alignment of two short period eclipsing binary systems

Tony Wells [1]★ B. C. Addison [1,2] R. A. Wittenmyer [1] Duncan J. Wright,[1] Tyler R. Fairnington,[1] Jason Dittmann,[3] Jonathan Horner,[1] Stephen R. Kane,[4] John Kielkopf,[5] Peter Plavchan [6] and Avi Shporer[7]

[1]*University of Southern Queensland, Centre for Astrophysics, West St, Toowoomba, QLD 4350, Australia*
[2]*Swinburne University of Technology, Centre for Astrophysics and Supercomputing, John Street, Hawthorn, VIC 3122, Australia*
[3]*Department of Astronomy, University of Florida, 211 Bryant Space Science Center, Gainesville, FL 32611, USA*
[4]*Department of Earth and Planetary Sciences, University of California, Riverside, CA 92521, USA*
[5]*Department of Physics and Astronomy, University of Louisville, Louisville, KY 40292, USA*
[6]*Department of Physics and Astronomy, George Mason University, 4400 University Drive MS 3F3, Fairfax, VA 22030, USA*
[7]*Department of Physics and Kavli Institute for Astrophysics and Space Research, Massachusetts Institute of Technology, Cambridge, MA 02139, USA*

ABSTRACT

We present a joint analysis of *TESS* photometry and radial velocity measurements obtained from the Minerva–Australis facility for two short-period eclipsing binaries, TIC 48227288 and TIC 339607421. TIC 339607421 hosts an M-dwarf companion ($M_B = 0.294 \pm 0.013\,\mathrm{M_\odot}$, $R_B = 0.291 \pm 0.006\,\mathrm{R_\odot}$) orbiting an F6V star ($M_A = 1.09 \pm 0.04\,\mathrm{M_\odot}$, $R_A = 1.21^{+0.03}_{-0.02}\,\mathrm{R_\odot}$), while TIC 48227288 contains a late K class companion ($M_B = 0.635 \pm 0.037\,\mathrm{M_\odot}$, $R_B = 0.605 \pm 0.011\,\mathrm{R_\odot}$) orbiting an F3V star ($M_A = 1.36^{+0.06}_{-0.08}\,\mathrm{M_\odot}$, $R_A = 1.61 \pm 0.03\,\mathrm{R_\odot}$). Both companions follow short period, near-circular orbits (P_B = 2.4–3.0 d, $e \approx 0.001$). Sky-projected obliquities for each system were derived using a classical analysis of the RV perturbation and the Reloaded Rossiter–McLaughlin (RRM) technique. The classical method indicates minor spin–orbit misalignment for both systems ($\lambda_A = -14.7^{+5.4\,\circ}_{-5.9}$ and $-17.8^{+1.9\,\circ}_{-2.0}$ for TIC 339607421 and TIC 48227288, respectively). The RRM analysis yields smaller obliquities ($\lambda_A = -8.2 \pm 0.2^\circ$ and $-9.5 \pm 0.2^\circ$ respectively), but confirms the minor misalignment inferred from the classical analysis. The findings of misaligned, circular orbits are notable even though the misalignments are not large, and suggest potential gaps in current models of binary formation and orbital evolution. As such, further investigation of these and similar systems appears warranted.

Key words: techniques: photometric – techniques: radial velocities – techniques: spectroscopic – binaries: eclipsing – stars: fundamental parameters – stars: low-mass.

1 INTRODUCTION

The concept of gravitationally bound multiple star systems dates back to the latter half of the 18th century, when John Michell applied statistical methods to argue that double or multiple stars, rather than being mere chance alignments, were much more likely to be in close physical proximity (Michell 1767). Soon after, William Herschel cataloged over 700 binaries, (Herschel & Watson 1782; Herschel 1785), before proposing that such stars orbit one another (Herschel 1802). Around the same time John Goodricke, (Goodricke 1783, 1784), attributed the periodic dimming of β Persei to the regular eclipsing of the star by a close, unseen orbiting companion – a foundational insight for the study of eclipsing binaries.

Multiple star systems are now known to be common: approximately 44 per cent of all FGK stars, 26 per cent of M class stars and $\gtrsim$60–80 per cent of early type stars exist in multiple configurations (Duchêne & Kraus 2013; Winters et al. 2019). High multiplicity is also observed among pre-main sequence stars (e.g. Mathieu 1994; Simon 1995; Ghez et al. 1997; Tohline 2002). Despite this prevalence, our understanding of the processes that lead to the formation of such systems is incomplete. Three principal formation pathways have been identified (Tohline 2002; Duchêne & Kraus 2013; Tokovinin & Moe 2020; Kuruwita & Haugbølle 2023): (1) Core fragmentation of turbulent pre-stellar cores during, or shortly after, the free fall collapse phase; (2) Disc fragmentation via gravitational instability within massive circumstellar discs; and (3) Dynamical capture of single, unbound stars formed in nearby stellar systems. Core fragmentation is believed to produce wide binaries (with separations of ∼100 to ∼10 000 au), whereas disc fragmentation results in closer binaries on the scale of the disc radius (<100 au) (Kuruwita & Haugbølle 2023). It is widely acknowledged that these initial orbital configurations can subsequently evolve due to interactions with tertiary companions (Kozai 1962), circumstellar disks (Tokovinin & Moe 2020), and the galactic tidal field (Priyatikanto et al. 2016), or following the ejection of a third body from the system (Armitage & Clarke 1997).

This study focuses on two close binary systems with orbital periods of 2–3 d which current theory suggests are likely products of disc

★ E-mail: tony.wells@usq.edu.au

**Table 1.** Details of *TESS* observations of TIC 48227288 and TIC 339607421.

	Camera	CCD chip	Dates
TIC 48227288			
Sector 11	1	3	April 23–May 20, 2019
Sector 38	1	4	April 29–May 26, 2021
Sector 65	1	4	May 4–May 30, 2023
TIC 339607421			
Sector 2	3	4	Aug. 23–Sept. 20, 2018
Sector 4	3	3	Oct. 19–Nov. 14, 2018
Sector 29	3	4	Aug. 29–Sept. 21, 2020
Sector 30	3	2	Sept. 23–Oct. 20, 2020
Sector 69	3	1	Aug. 25–Sept. 20, 2023

fragmentation. At first glance, it would therefore seem likely that the spin and orbital axes of each member of the binary would be aligned as they originate from the same regions of their respective molecular clouds. However, as noted by Albrecht et al. (2012a), the primary and companion stars would have been significantly larger during the pre-main sequence phase thereby precluding the existence of such compact orbits at that time. The close proximity therefore suggests that significant orbital evolution has taken place post-formation.

Orbital evolution may involve chaotic processes known to produce spin–orbit misalignment, including Kozai–Lidov interactions with a wide orbiting tertiary body (Kozai 1962), disc warping during accretion (Bate, Lodato & Pringle 2010) or magnetic interaction between the two stars and the circumstellar disc (Lai, Foucart & Lin 2011). Alternatively, close binaries may be produced by accretion driven inward migration following disk fragmentation (Tokovinin & Moe 2020). Measuring spin–orbit alignment (obliquity) in these systems should therefore constrain formation and evolutionary pathways: low obliquities suggest quiescent histories (or later alignment via tidal interactions), whereas high obliquities imply a more chaotic formation history.

Obliquities are now commonly measured in exoplanet systems, (see for example Addison et al. 2013, 2016; Clark et al. 2023), yet relatively few studies have explored spin–orbit alignment in stellar binaries. This is somewhat surprising given that obliquity is commonly determined by examination of the Rossiter–McLaughlin (RM) effect, which was first observed a century ago in the β Lyrae (Rossiter 1924) and Algol (McLaughlin 1924) systems. The paucity of binary star obliquity studies stems from two main factors: (1) instrument precision has only recently improved to the point that the measurement of spin orbit alignment for more slowly rotating stars is possible (Triaud et al. 2013) and, (2) binary system spectra are often contaminated by light from the companion, complicating interpretation (there is no such issue when observing transiting exoplanets). To mitigate the latter complication, we follow the strategy of Triaud et al. (2013) and focus on single-lined eclipsing binaries (SB1s). This approach naturally leads to the study of binary star systems with large mass ratios and allows comparison to formation pathways more commonly observed in the establishment of brown dwarf and exoplanetary systems.

The RM effect manifests as distortions in rotationally broadened absorption lines during eclipses, when the transiting companion sequentially obscures blue and red shifted limbs of the host star. These distortions allow reconstruction of the path of the occulting body. Traditionally, obliquities are inferred from the perturbation in radial velocities arising from the resulting movement in the spectral line centroid (Triaud 2018). More recent approaches, including Doppler tomography (Zhou et al. 2016a, b, 2017) and the Reloaded RM (RRM) (Cegla et al. 2016; Bourrier et al. 2020; Kunovac Hodžić et al. 2021; Doyle et al. 2023), directly model distortions. Doppler tomography involves fitting a spectral model to the disk integrated lines to account for the signature of the companion while RRM isolates the stellar line occulted by the companion and directly determines the local RV centroid. Another direct analysis technique, RM revolutions (RMR), has recently been developed (Bourrier et al.
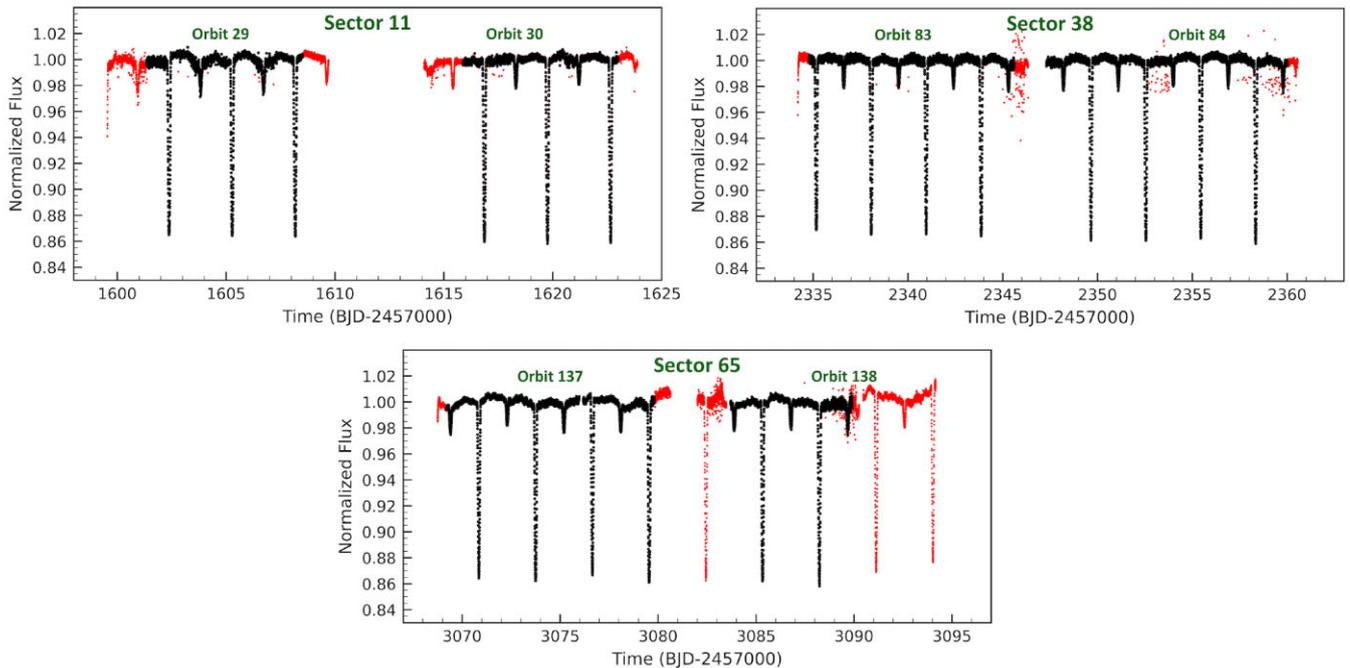
Figure 1. TIC 48227288 *TESS* PDCSAP light curves. Data shown in black were used in the joint ALLESFITTER analysis. Red data were excluded due to quality issues. The data shown in this figure are available online in machine readable format.
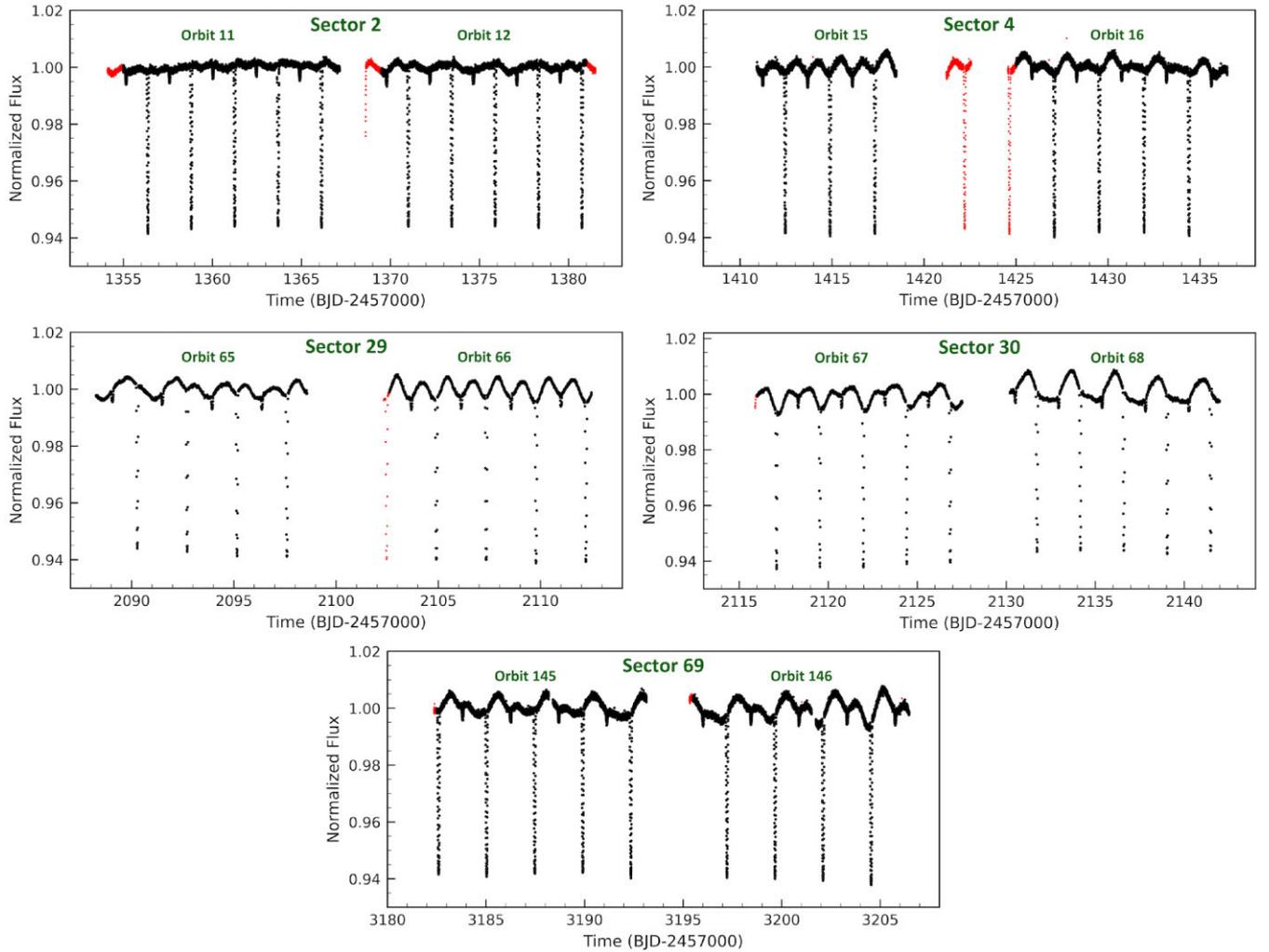
Figure 2. TIC 339607421 *TESS* PDCSAP light curves. Data shown in black were used in the joint ALLESFITTER analysis. Red data were excluded due to quality issues. The data shown in this figure are available online in machine readable format.

Table 2. TIC 48227288 radial velocities determined from MINERVA observations. 'RM' appended to an instrument entry indicates that the observation was made during an eclipse.

Time (BJD)	Velocity ($\mathrm{m\,s^{-1}}$)	Uncertainty ($\mathrm{m\,s^{-1}}$)	Instrument
2459757.044306	46 976	152	MINERVAT1
2459769.010814	56 657	141	MINERVAT1
2459786.95997	7544	144	MINERVAT1RM
2459795.988807	−33 469	147	MINERVAT1
2460008.183256	−45 992	206	MINERVAT1
2459757.044306	46 912	151	MINERVAT3
2459769.010814	56 459	154	MINERVAT3
2459786.95997	7182	148	MINERVAT3RM
2459795.988807	−33 722	153	MINERVAT3
2460008.183256	−46 072	164	MINERVAT3
2460021.263515	40 440	155	MINERVAT3
2460035.995702	12 467	181	MINERVAT3
2460036.014002	10 622	166	MINERVAT3RM
2460036.032255	8517	164	MINERVAT3RM
2460036.050509	6917	157	MINERVAT3RM
2460036.068762	5093	166	MINERVAT3RM

Note. The above table is published in full in machine readable form online. The portion shown here is to provide a guide to form and content.

Table 3. TIC 339607421 radial velocities determined from MINERVA observations. 'RM' appended to an instrument entry indicates that the observation was made during an eclipse.

Time (BJD)	Velocity ($\mathrm{m\,s^{-1}}$)	Uncertainty ($\mathrm{m\,s^{-1}}$)	Instrument
2459845.02718	26 843	237	MINERVAT1
2459916.981703	2708	288	MINERVAT1
2459922.065061	−12 999	253	MINERVAT1
2459928.930804	25 874	224	MINERVAT1
2459933.016964	43 458	238	MINERVAT1
2459941.977936	−18 524	257	MINERVAT1
2459952.957495	50 274	233	MINERVAT1
2459980.948251	−19 570	253	MINERVAT1
2459922.065061	−12 873	237	MINERVAT3
2459933.016964	43 960	213	MINERVAT3
2459952.957495	50 078	216	MINERVAT3
2459980.948251	−19 320	247	MINERVAT3
2460021.886871	−2292	240	MINERVAT3
2460136.194679	23 296	251	MINERVAT3
2460136.217365	20 752	258	MINERVAT3RM
2460136.240028	19 564	256	MINERVAT3RM

Note. The above table is published in full in machine readable form online. The portion shown here is to provide a guide to form and content.
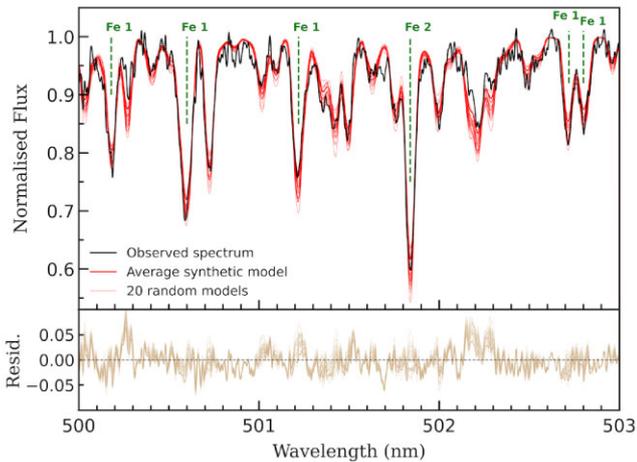
Figure 3. An example of the fit between the optimum ISPEC spectrum and a TIC 48227288A spectrum observed by MINERVA-Australis. The bold red line is the best-fitting model spectra. 20 model spectra drawn from random sampling of the model parameter distributions are shown as fainter red lines.
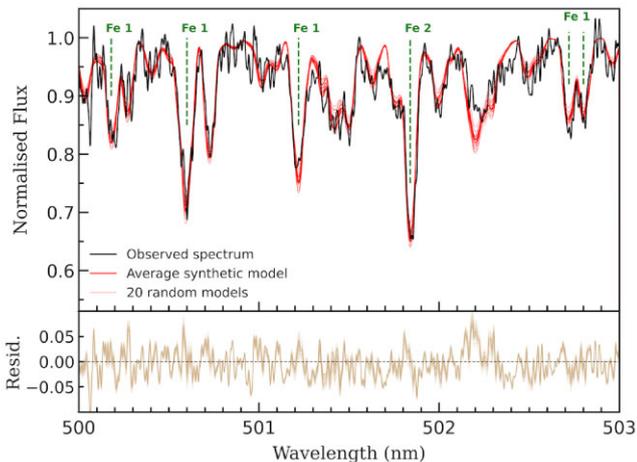
Figure 4. An example of the fit between the optimum ISPEC spectrum and a TIC 339607421A spectrum observed by MINERVA-Australis. The bold red line is the best fit model spectra. 20 model spectra drawn from random sampling of the model parameter distributions are shown as fainter red lines.

2021) for systems with small companions that are less suitable for RRM analysis.

Table A1, (partially reproduced from Albrecht et al. 2011), lists obliquity measurements reported for stellar binaries. Early studies are dominated by quantitative (aligned/misaligned) estimates of spin–orbit alignment (see for example Twigg 1979). In an early quantitative study, Hale (1994) examined 73 multiple star systems and concluded that all solar-type binary systems with separations less than 40 au were generally aligned. However, a re-analysis, (Justesen & Albrecht 2020), cast doubt on Hale's findings and thus they have been omitted from Table A1. More recent surveys include the BANANA ('Binaries Are Not Always Neatly Aligned') project (Albrecht et al. 2007, 2009, 2011, 2013, 2014; Winn et al. 2011) which modelled the RM effect observed for hot binary systems comprising stars of similar masses, and the EBLM ('Eclipsing Binary, Low Mass') project, (Triaud et al. 2013; Kunovac Hodžić et al. 2020), where RRM has been employed to derive obliquities for systems containing low mass companion stars. Other methods used to determine binary star

obliquity include apsidal motion (Marcussen & Albrecht 2022), and gravity darkening (Zhou & Huang 2013; Ahlers, Seubert & Barnes 2014; Liang, Winn & Albrecht 2022). While most results indicate aligned configurations, exceptions exist, including AI Phe (Sybilski et al. 2018), CV Velorum (Albrecht et al. 2014) and DI Herculis (Albrecht et al. 2009; Philippov & Rafikov 2013; Liang et al. 2022). More recently, studies of binary star populations with periods ranging from 50 to 3000 d, (Marcussen et al. 2024; Smith, Moe & Kratter 2024), suggest that the likelihood of misalignment increases with increasing eccentricity for these wide orbiting systems.

In this work, we expand the current sample of binary system obliquity measurements by analysing two SB1 systems: TIC 48227288 and TIC 339607421. We derive sky-projected obliquities (λ) and orbital parameters from joint analyses of photometric data collected by NASA's *Transiting Exoplanet Survey Satellite* (*TESS*) and ground-based spectroscopic observations carried out at the MINERVA-Australis facility. Two approaches are taken to estimate obliquity. Obliquities are first obtained through a classical analysis of the RV perturbation. Further obliquity estimates are then derived from a more direct analysis of the spectroscopic data via the RRM technique. The structure of this paper is as follows: Section 2 details the observational data and reduction methods; Section 3 presents stellar parameters and joint analysis results; Section 4 discusses our findings in context of previous studies; and Section 5 summarizes our main conclusions.

2 OBSERVATIONS

Space-based photometric observations of the two target systems were conducted intermittently over several years using *TESS* (Section 2.1) with high resolution spectroscopic observations subsequently carried out at the MINERVA-Australis observatory (Section 2.2). Observation details and data processing procedures are presented below.

2.1 *TESS* photometry

TESS observed TIC 48227288 in sectors 11, 38, and 65 and TIC 339607421 in sectors 2, 4, 29, 30, and 69. Cameras and CCD chips used, along with the corresponding observation windows, are listed in Table 1. All TIC 48227288 observations were obtained in 120 s cadence mode. A total of 23 primary and 24 secondary eclipses were recorded for TIC 48227288 with depths of ~135 and ~20 ppt, respectively (Fig. 1). TIC 339607421 was observed in 120 s cadence mode in sectors 2, 4, and 69 and 600 s cadence mode in sectors 29 and 30. A total of 47 primary and 45 secondary eclipses were observed for this target, with depths of approximately 60 and 5 ppt, respectively (Fig. 2).

For both systems we used Pre-search Data Conditioning Simple Aperture Photometry (*PDCSAP*) photometric data retrieved using the LIGHTKURVE[1] package (Lightkurve Collaboration 2018). Data points with non-zero quality flags were removed, and any partially observed eclipses excluded. Intra-sector gaps in data continuity (e.g. due to momentum dumps) were identified, and light curve segments between such gaps independently normalized using LIGHTKURVE routines (black points in Figs 1 and 2). For modelling purposes, the TIC 48227288 photometric data were treated as six independent data sets, while the TIC 339607421 data were divided into ten independent segments.

---

[1] https://github.com/lightkurve/lightkurve

Table 4. Stellar properties for TIC 48227288A and TIC 339607421A. Notes: [†] preferred solution; [‡] excluded from SED fitting process.

Property	TIC 48227288A	TIC 339607421A	Sources
Astrometric properties			
R.A. (hh:mm:ss)	03:04:50.27	03:04:50.27	Gaia DR3
Decl. (dd:mm:ss)	14:51:40.29	-52:33:30.85	Gaia DR3
μ_α (mas yr^{-1})	-58.409 ± 0.028	12.560 ± 0.013	Gaia DR3
μ_δ (mas yr^{-1})	-72.082 ± 0.024	52.692 ± 0.017	Gaia DR3
Parallax (mas)	9.9775 ± 0.0249	10.0183 ± 0.0132	Gaia DR3
Distance (pc)	$100.0473^{+0.2570}_{-0.2584}$ [†]	$99.6676^{+0.1221}_{-0.1264}$ [†]	Gaia DR3
	$100.0712^{+0.1839}_{-0.1401}$	$99.8724^{+0.1255}_{-0.0932}$	ARIADNE, Section 3.1
Photometric properties			
B_T (mag)	8.761 ± 0.017	9.524 ± 0.020	Tycho
V_T (mag)	8.273 ± 0.012	8.998 ± 0.016	Tycho
J (mag)	7.292 ± 0.020[‡]	7.978 ± 0.024	2MASS
H (mag)	7.083 ± 0.024[‡]	7.742 ± 0.069	2MASS
K (mag)	7.030 ± 0.029[‡]	7.705 ± 0.018	2MASS
TESS (mag)	7.778 ± 0.006	8.466 ± 0.006	TIC v8.2
WISE$_1$ (mag)	6.974 ± 0.035	7.604 ± 0.029	WISE
WISE$_2$ (mag)	6.981 ± 0.019	7.660 ± 0.020	WISE
Gaia (mag)	8.117 ± 0.003	8.824 ± 0.003	Gaia DR3
Gaia$_{BP}$ (mag)	8.346 ± 0.003	9.069 ± 0.003	Gaia DR3
Gaia$_{RP}$ (mag)	7.721 ± 0.004	8.415 ± 0.004	Gaia DR3
Johnson V (mag)	8.211 ± 0.014	8.921 ± 0.017	ACSS v3
Johnson B (mag)	8.699 ± 0.018	9.449 ± 0.018	ACSS v3
Spectroscopic properties			
Spectral type	F5	F8	HD catalogue
	F3V[†]	F6V[†]	ARIADNE, Section 3.1
$T_{\mathrm{eff,A}}$ (K)	6816 ± 134	6327 ± 128	TIC v8.2
	6723^{+104}_{-97} [†]	6402^{+39}_{-65} [†]	ARIADNE, Section 3.1
$\log g_A$ (cgs)	4.17 ± 0.09	4.34 ± 0.08	TIC v8.2
	4.16 ± 0.02	$4.31^{+0.02}_{-0.01}$	ARIADNE, Section 3.1
Metallicity, [M/H]$_A$	-0.09 ± 0.11	-0.27 ± 0.05	ISPEC, Section 3.1
Metallicity, [Fe/H]$_A$	$-0.03^{+0.06}_{-0.07}$	-0.15 ± 0.03	ARIADNE, Section 3.1
$\upsilon_A \sin i$ (km s^{-1})	20.0 ± 1.7	24.6 ± 0.6	ISPEC, Section 3.1
	19.0 ± 0.9	26.0 ± 2.2	ALLESFITTER, Section 3.2
	17.9 ± 0.2 [†]	24.9 ± 0.2 [†]	Reloaded RM, Section 3.3
Derived stellar properties			
M_A (M$_\odot$)	1.47 ± 0.11	1.25 ± 0.18	TIC v8.2
	$1.36^{+0.06}_{-0.08}$ [†]	1.09 ± 0.04 [†]	ARIADNE, Section 3.1
R_A (R$_\odot$)	1.64 ± 0.07	1.25 ± 0.05	TIC v8.2
	1.61 ± 0.03[†]	$1.21^{+0.03}_{-0.02}$ [†]	ARIADNE, Section 3.1
ρ_A (cgs)	0.47 ± 0.11	0.89 ± 0.20	TIC v8.2
	0.46 ± 0.02 [†]	$0.88^{+0.04}_{-0.03}$ [†]	ARIADNE, Section 3.1
Age (Gyr)	$2.3^{+0.8}_{-0.6}$	$4.3^{+1.0}_{-4.2}$	ARIADNE, Section 3.1

Note. Source references: 2MASS (Cutri et al. 2003); ALLESFITTER (Günther & Daylan 2021); ACSS v3 (Kharchenko 2001); ARIADNE (Vines & Jenkins 2022); GAIA DR3 (Gaia Collaboration 2023); HD catalogue (Cannon & Pickering 1993); ISPEC (Blanco-Cuaresma et al. 2014); TIC v8.2 (Stassun et al. 2019); Tycho (Høg et al. 2000); WISE (Cutri et al. 2021);

2.2 MINERVA spectroscopy

High resolution spectroscopic observations of TIC 48227288 and TIC 339607421 were conducted at the MINERVA-Australis facility, located at the Mt Kent Observatory in Queensland, Australia (Wittenmyer et al. 2018; Addison et al. 2019). The facility comprises an array of remotely accessible, independent 0.7 m PlaneWave CDK700 telescopes. Four telescopes, (T1, T3, T4 and T5), simultaneously feed starlight via fiber optics to a shared KiwiSpec R4-100 high resolution spectrograph, operating at a resolution of R ≈ 80 000 over a wavelength range of 480 to 630 nm.

TIC 48227288 was observed across 129 epochs between 2022 June 26 and 2023 August 31, including coverage of primary eclipses that took place on 2023 April 1st, (10 observations on T3 and 6 on T4), and 2023 April 30th, (9 observations on T3 and 10 on T4).

TIC 339607421 was observed over 144 epochs from 2022 September 22 to 2023 September 9, including coverage of primary eclipses
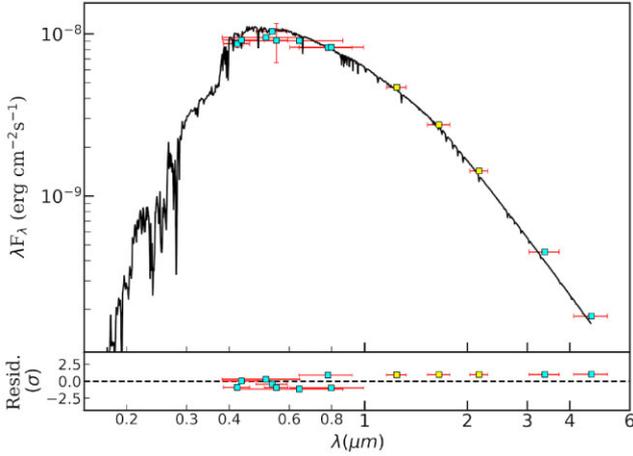
Figure 5. Top: TIC 48227288A best-fitting SED obtained from the ARIADNE analysis. Black line is the best model fit. Blue squares show photometry data used in determining the SED profile while yellow squares show data excluded from the fitting process due to possible quality issues. Horizontal bars correspond to the filter band-pass width while vertical error bars reflect magnitude uncertainties. Bottom: residuals relative to flux uncertainties.
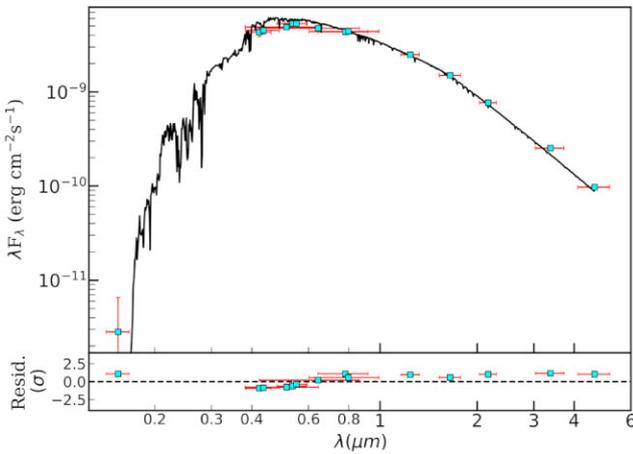
Figure 6. Top: TIC 339607421A best-fitting SED obtained from the ARIADNE analysis. Black line is the best model fit. Blue squares show photometry data used in determining the SED profile. Horizontal bars correspond to the filter band-pass width while vertical error bars reflect magnitude uncertainties. Bottom: Residuals relative to flux uncertainties.

on 2023 July 10, (10 observations on T3 and 9 each on T4 and T5), 2023 August 23, (6 observations on T3 and 7 on T4), and 2023 September 9, (10 observations each on T3 and T4).

Two simultaneous calibration fibers, illuminated by a quartz lamp shining through an iodine cell, were used to monitor and correct instrumental drifts. Radial velocities (RVs) were extracted by cross-correlating each spectrum with a synthetic mask chosen to closely match the primary stellar type as determined via ISPEC/ARIADNE analysis (see Section 3.1). An F3V mask was used in the analysis of TIC 48227288 spectra and an F6V mask for TIC 339607421. Final RV measurements are provided in Tables 2 and 3. In this study, radial velocities originating from the individual MINERVA telescopes are modelled on the assumption that they originate from independent instruments.

3 ANALYSIS

3.1 Primary star characterization

Before companion stars properties (hereafter denoted with subscript 'B') can be accurately determined, primary star parameters (designated with subscript 'A') must be accurately determined. The following procedure was adopted to determine the primary star parameters.

To begin the primary star characterization process, the 10 highest signal-to-noise ratio (SNR) MINERVA spectra were selected for each target to be analyzed using the ISPEC software package[2] (Blanco-Cuaresma et al. 2014; Blanco-Cuaresma 2019). Spectra were first set in the rest frame before blaze corrections to individual orders were performed using flat field observations carried out previously at MINERVA-Australis. Sections of the spectra likely to be affected by telluric contamination were then removed using the ISPEC telluric filter with margins set to the default value of ± 30 km s^{-1}. Subsequent normalization of the spectra was complicated by the presence of a pronounced Hβ absorption feature (~ 484 to 488 nm) that dominated the first order of the MINERVA spectra and hindered spline-based continuum fitting. To address this, a two step normalization process was adopted: First, an approximate normalization of the continuum was performed using the ISPEC spline function and initial estimates of the primary star's effective temperature, $T_{eff,A}$, overall metallicity, $[M/H]_A$, surface gravity, $\log g_A$, and projected rate of rotation, $\upsilon_A \sin i$ determined using ISPEC's grid-modelling routine. A synthetic spectral analysis was then performed to obtain an initial estimate the metallicity, $[Fe/H]_A$.

The initial parameter estimates were then used to generate a synthetic spectrum which enabled a better normalization of the original MINERVA spectra to be performed before $T_{eff,A}$, $\log g_A$, $[M/H]_A$, $\upsilon_A \sin i$ and $[Fe/H]_A$ were re-estimated. This procedure was repeated across the 10 selected spectra. Final stellar parameters were taken as the mean of the individual estimates obtained for each spectra, with standard deviations adopted as uncertainties. The resulting model spectra provided excellent fits to the observed MINERVA data, (see Figs 3 and 4).

To further refine the primary star characteristics, the averaged ISPEC outcomes were used as priors in the spectral energy distribution (SED) fitting program, ARIADNE[3] (Vines & Jenkins 2022), along with some additional photometric and astrometric data. The additional input included *Gaia* DR3 parallax and G, G_R, and G_{RP} magnitudes (Gaia Collaboration 2023); TYCHO B_T and V_T magnitudes (Høg et al. 2000); 2MASS J, H, K magnitudes (Cutri et al. 2003); WISE W_1 and W_2 magnitudes (Cutri et al. 2021); and APASS Johnson B and V magnitudes (Henden et al. 2015). Magnitude data flagged as potentially contaminated, (e.g. by the diffraction spikes from a neighboring stars), were excluded from the fit.

Normal priors were adopted for $T_{eff,A}$, $[M/H]_A$ and $\log g_A$ based on the ISPEC results, while default priors were employed for distance (as estimated from Gaia EDR3; Bailer-Jones et al. 2021), radius (uniform prior from 0.5 to $20 R_\odot$) and line of sight extinction, Av, (uniform prior from 0 to the maximum line-of-sight value). Stellar properties were derived from Bayesian model averaging across four atmospheric models: BT-Settl (Schlafly & Finkbeiner 2011), Phoenix V2 (Husser et al. 2013), Kurucz (Kurucz 1993), and

---

[2] https://github.com/marblestation/iSpec
[3] https://github.com/jvines/astroARIADNE

Table 5. Median and 68 per cent confidence intervals of astrophysical parameters derived for TIC 48227288 by ALLESFITTER. Priors are shown as uniform $\mathcal{U}$(a,b) or normal $\mathcal{N}(\mu, \sigma)$. Additional parameters derived for the eclipse and radial velocity fits can be found in Table B1. Notes:[†] preferred solution. [‡] prior not used for flattened light curve model.

Parameter	Prior	Best fit[†]	Best fit (flattened light curve)
Fitted parameters			
Radius ratio, R_B/R_A	$\mathcal{U}(0.3, 0.4)$	0.3756 ± 0.0011	0.3747 ± 0.0009
Radii sum to semi-major axis, $(R_A + R_B)/a$	$\mathcal{U}(0.1, 0.3)$	$0.2096^{+0.0007}_{-0.0010}$	0.2101 ± 0.0005
Cosine of inclination, $\cos i_B$	$\mathcal{U}(0, 0.4)$	$0.1032^{+0.0009}_{-0.0010}$	$0.1032^{+0.0006}_{-0.0007}$
Mid transit time $T_{0;B}$ (BJD$_{\text{TDB}}$-2459000)	$\mathcal{U}(395.0, 397.0)$	395.99372 ± 0.00002	395.99380 ± 0.00001
Orbital period, P_B (d)	$\mathcal{U}(2.796, 2.996)$	2.8963969 ± 0.0000001	2.8963965 ± 0.0000001
$\sqrt{e_B}\cos\omega_B$	$\mathcal{U}(-0.5, 0.5)$	$-0.027^{+0.007}_{-0.003}$	$-0.019^{+0.004}_{-0.005}$
$\sqrt{e_B}\sin\omega_B$	$\mathcal{U}(-0.5, 0.5)$	$0.021^{+0.022}_{-0.029}$	$0.047^{+0.013}_{-0.016}$
Radial velocity semi-amplitude, K_B (km s^{-1})	$\mathcal{U}(53.0, 63.0)$	$58.62^{+0.13}_{-0.14}$	$58.47^{+0.14}_{-0.15}$
Surface brightness ratio, J_B	$\mathcal{U}(0, 1)$	$0.1375^{+0.0006}_{-0.0007}$	0.1417 ± 0.0004
Doppler beaming amplitude, A_{beaming} (ppt)	$\mathcal{U}(0, 1)$[‡]	$0.221^{+0.011}_{-0.012}$	–
Atmospheric amplitude, $A_{\text{atmosphere}}$ (ppt)	$\mathcal{U}(0, 1)$[‡]	$0.011^{+0.012}_{-0.008}$	–
Ellipsoidal amplitude, $A_{\text{ellipsoidal}}$ (ppt)	$\mathcal{U}(0, 5)$[‡]	2.915 ± 0.026	–
Stellar rotational velocity, $v_A \sin i$ (km s^{-1})	$\mathcal{N}(20, 8.5)$	19.0 ± 0.9	19.2 ± 0.9
Sky projected obliquity, λ (deg)	$\mathcal{U}(-180, 180)$	$-17.8^{+1.9}_{-2.0}$	$-17.5^{+2.1}_{-2.2}$
Derived parameters			
Primary radius to semi-major axis, R_A/a	–	$0.1524^{+0.0005}_{-0.0007}$	0.1528 ± 0.0003
Mass ratio, q	–	0.469 ± 0.013	0.469 ± 0.013
Companion radius, R_B (R$_\odot$)	–	0.605 ± 0.011	0.604 ± 0.011
Companion mass, M_B (M$_\odot$)	–	0.635 ± 0.037	$0.635^{+0.037}_{-0.038}$
Companion density, ρ_B (g cm^{-3})	–	$4.04^{+0.42}_{-0.38}$	$4.07^{+0.42}_{-0.38}$
Eccentricity, e_B	–	$0.0013^{+0.0011}_{-0.0003}$	$0.0026^{+0.0013}_{-0.0010}$
Argument of periastron, w_B (deg)	–	$142.5^{+52.9}_{-27.7}$	$111.8^{+15.5}_{-7.6}$
Orbital semi-major axis, a (AU)	–	$0.04916^{+0.00094}_{-0.00093}$	0.04901 ± 0.00092
Orbital inclination, i_B (deg)	–	$84.08^{+0.06}_{-0.05}$	84.07 ± 0.04
Primary transit depth (ppt) $\delta_{\text{tra:TESS}}$	–	$134.41^{+0.08}_{-0.10}$	134.54 ± 0.07
Primary transit impact parameter, $b_{\text{tra;B}}$	–	0.676 ± 0.004	0.674 ± 0.003
Primary transit total duration, $T_{\text{tot;B}}$ (d)	–	$0.1700^{+0.0004}_{-0.0006}$	0.1702 ± 0.0003
Primary transit full duration, $T_{\text{full;B}}$ (d)	–	–	–
Secondary transit depth (ppt) $\delta_{\text{occ:TESS}}$	–	$18.55^{+0.08}_{-0.07}$	18.97 ± 0.05
Secondary transit epoch, $T_{0;\text{occ;B}}$ (BJD$_{\text{TDB}}$-2459000)	–	394.54374 ± 0.00015	394.54384 ± 0.00011
Secondary transit impact parameter, $b_{\text{occ;B}}$	–	$0.678^{+0.004}_{-0.005}$	$0.677^{+0.003}_{-0.004}$

Castelli/Kurucz (Castelli & Kurucz 2003). For TIC 339607421A, however, the Kurucz model yielded significantly discrepant results and was therefore excluded from the average.

Final primary star parameters are reported in Table 4. The model SED fits based on the Castelli/Kurucz atmospheric model are shown in Figs 5 and 6 for TIC 48227288A and TIC 339607421A, respectively. Although the 2MASS J, H, K data for TIC 48227288A were excluded from the analysis due to potential contamination, comparison with the model SED showed good agreement (see yellow points in Fig. 5).

Our analysis suggests that TIC 48227288A is a main-sequence F3 class star with a radius of 1.61 ± 0.03 R$_\odot$, mass of $1.36^{+0.06}_{-0.08}$M$_\odot$, effective temperature of 6723^{+104}_{-97} K, and close to solar metallicity, [Fe/H]$_A = -0.03^{+0.06}_{-0.07}$, with an estimated age of ~2–3 Gyr. TIC 339607421A, on the other hand, is a slightly metal poor, [Fe/H]$_A = -0.15 \pm 0.03$, main sequence F6 star with a radius of

$1.21^{+0.03}_{-0.02}$ R$_\odot$, mass of 1.09 ± 0.04 M$_\odot$ with an effective temperature of 6402^{+39}_{-65} K, and likely aged less than 5 Gyr. These results are consistent, within uncertainties, with the TIC 48227288 and TIC 339607421 parameters listed in version 8.2 of the *TESS* input catalogue (Stassun et al. 2019) and as such, were the parameters we used when characterizing the companion stars in each system.

3.2 ALLESFITTER joint analysis of light curve and RV data

To determine the properties of the companion stars and the stellar obliquities of the host stars, we first performed a joint analysis of the *TESS* photometric and MINERVA spectroscopic data using the ALLESFITTER package[4] (Günther & Daylan 2019, 2021). This

[4]https://github.com/MNGuenther/allesfitter

Table 6. Median and 68 per cent confidence intervals of astrophysical parameters derived for TIC 339607421 by ALLESFITTER. Priors are shown as uniform $\mathcal{U}$(a,b) or normal $\mathcal{N}(\mu, \sigma)$. Additional parameters derived for the eclipse and radial velocity fits can be found in Table B2. Notes:[†] preferred solution. [‡] prior not used for flattened light curve model.

Parameter	Prior	Best fit	Best fit (flattened light curve)[†]
Fitted parameters			
Radius ratio, R_B/R_A	$\mathcal{U}(0.23, 0.25)$	$0.2388^{+0.0010}_{-0.0009}$	$0.2395^{+0.0005}_{-0.0006}$
Radii sum to semi-major axis, $(R_A + R_B)/a$	$\mathcal{U}(0.17, 0.19)$	$0.1793^{+0.0006}_{-0.0007}$	0.1788 ± 0.0004
Cosine of inclination, $\cos i_B$	$\mathcal{U}(0, 0.2)$	$0.1056^{+0.0008}_{-0.0009}$	0.1058 ± 0.0005
Mid transit time $T_{0;B}$ (BJD$_{TDB}$-2459000)	$\mathcal{U}(282.7, 283.0)$	282.89461 ± 0.00003	282.89468 ± 0.00001
Orbital period, P_B (d)	$\mathcal{U}(2.438, 2.439)$	$2.43821227 \pm 0.00000007$	$2.43821243 \pm 0.00000002$
$\sqrt{e_B} \cos \omega_B$	$\mathcal{U}(-0.5, 0.5)$	$0.005^{+0.008}_{-0.007}$	0.017 ± 0.005
$\sqrt{e_B} \sin \omega_B$	$\mathcal{U}(-0.5, 0.5)$	$-0.004^{+0.029}_{-0.031}$	$-0.015^{+0.037}_{-0.027}$
Radial velocity semi-amplitude, K_B (km s^{-1})	$\mathcal{U}(36, 38)$	36.84 ± 0.14	$36.85^{+0.13}_{-0.12}$
Surface brightness ratio, J_B	$\mathcal{U}(0, 1)$	$0.0649^{+0.0009}_{-0.0010}$	$0.0696^{+0.0004}_{-0.0003}$
Doppler beaming amplitude, $A_{beaming}$ (ppt)	$\mathcal{U}(0, 5)$[‡]	1.153 ± 0.009	–
Atmospheric amplitude, $A_{atmosphere}$ (ppt)	$\mathcal{U}(0, 5)$[‡]	0.497 ± 0.020	–
Ellipsoidal amplitude, $A_{ellipsoidal}$ (ppt)	$\mathcal{U}(0, 5)$[‡]	2.051 ± 0.020	–
Stellar rotational velocity, $v_A \sin i$ (km s^{-1})	$\mathcal{N}(24.6, 3.0)$	$25.8^{+2.2}_{-2.1}$	26.0 ± 2.2
Sky projected obliquity, λ (deg)	$\mathcal{U}(-180, 180)$	$-15.3^{+5.3}_{-5.5}$	$-14.7^{+5.4}_{-5.9}$
Derived parameters			
Primary radius to semi-major axis, R_A/a	–	0.1447 ± 0.0006	0.1442 ± 0.0004
Mass ratio, q	–	0.271 ± 0.007	0.270 ± 0.007
Companion radius, R_B (R$_\odot$)	–	0.290 ± 0.006	0.291 ± 0.006
Companion mass, M_B (M$_\odot$)	–	$0.295^{+0.014}_{-0.013}$	0.294 ± 0.013
Companion density, ρ_B (g cm^{-3})	–	$17.10^{+1.72}_{-1.59}$	$16.90^{+1.67}_{-1.55}$
Eccentricity, e_B	–	$0.0005^{+0.0014}_{-0.0004}$	$0.0010^{+0.0011}_{-0.0004}$
Argument of periastron, w_B (deg)	–	$256.6^{+39.8}_{-188.7}$	$285.1^{+33.3}_{-243.1}$
Orbital semi-major axis, a (AU)	–	$0.03898^{+0.00085}_{-0.00079}$	$0.03911^{+0.00083}_{-0.00079}$
Orbital inclination, i_B (deg)	–	83.94 ± 0.05	83.93 ± 0.03
Primary transit depth (ppt) $\delta_{tra:TESS}$	–	$56.56^{+0.07}_{-0.08}$	56.66 ± 0.02
Primary transit impact parameter, $b_{tra;B}$	–	0.730 ± 0.004	0.734 ± 0.001
Primary transit total duration, $T_{tot;B}$ (d)	–	0.1135 ± 0.0003	0.1129 ± 0.0001
Primary transit full duration, $T_{full;B}$ (d)	–	–	–
Secondary transit depth (ppt) $\delta_{occ:TESS}$	–	4.18 ± 0.05	3.98 ± 0.02
Secondary transit epoch, $T_{0;occ;B}$ (BJD$_{TDB}$-2459000)	–	$284.11389^{+0.00033}_{-2.43845}$	284.11462 ± 0.00011
Secondary transit impact parameter, $b_{occ;B}$	–	0.729 ± 0.004	$0.733^{+0.002}_{-0.003}$

analysis incorporated the host star properties determined earlier from the ISPEC and ARIADNE modelling.
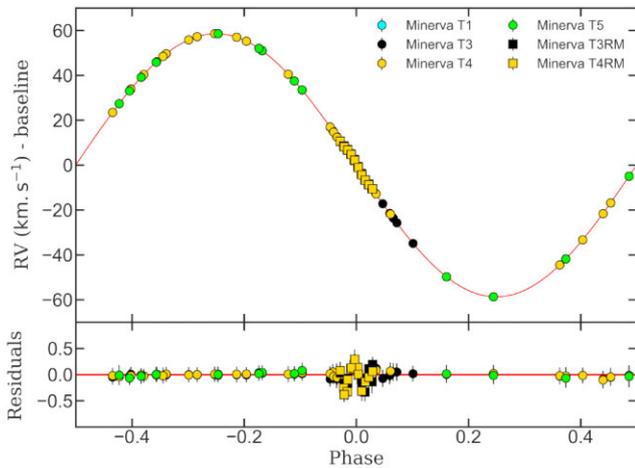
The priors used in the ALLESFITTER joint analyses are listed in Tables 5, 6, B1, and B2. Generous uniform priors were applied to all parameters except for $v \sin i$ where a 5σ (weak) normal prior was employed that was centered on $v \sin i$ estimates obtained from the ISPEC analysis of the MINERVA spectra, ($\mathcal{N}(20.0, 8.5)$ km s^{-1} and $\mathcal{N}(24.6, 3.0)$ km s^{-1} for TIC 48227288 and TIC 339607421, respectively). Boundary conditions for several uniform priors, (mid eclipse time ($T_{0,B}$), ratio of the sum of star radii to semi major axis ($R_A + R_B$)/a_B, primary to secondary stellar radius ratio (R_B/R_A), cosine of the angle of orbital inclination ($\cos i_B$), orbital period (P_B), eccentricity ($\sqrt{e_B} \cos \omega_B$, $\sqrt{e_B} \sin \omega_B$) and radial velocity semi-amplitude (K_B)), were guided by exploratory modeling of the radial velocity and light curve data performed using RADVEL[5] (Fulton

et al. 2018) and the online version of EXOFAST[6] (Eastman, Gaudi & Agol 2013). Uniform prior ranges for light curve flux uncertainties ($\ln \sigma_F$) and radial velocity jitter ($\ln \sigma_{jitter}$) were informed by reported uncertainties in the *TESS* flux and MINERVA datasets. Following the recommendations of Espinoza & Jordán (2015), the priors for the transformed limb darkening coefficients (q_1, q_2) were set to $\mathcal{U}(0,1)$ as was the specific surface brightness ratios (J_B). A wide ranging prior was set for the sky projected obliquity, $\lambda_A, \mathcal{U}(-180, 180)$.

It is evident in Figs 1 and 2 that there is considerable baseline flux variability between eclipses. We modelled the variability as a combination of three effects outlined in Shporer (2017): (a) ellipsoidal distortion of the primary star induced by the tidal bulge raised on the primary surface by the close orbiting companion; (b) Doppler

[6]https://astroutils.astronomy.osu.edu/exofast/exofast.shtml

[5]https://github.com/California-Planet-Search/radvel

Figure 7. Phase folded radial velocity model for TIC 48227288 obtained from the ALLESFITTER analysis. Observations from each of the MINERVA telescopes are shown including observations made during the primary eclipse. The red line shown represents the best fit model. Residual velocities to the best-fitting model are shown in the bottom panel.

boosting (or beaming) modulations in which the observed flux is modulated by, for example, radial velocity induced Doppler shifting of the host spectrum; and (c) atmospheric brightness modulation, arising from reflected light and thermal emission from the companion. ALLESFITTER incorporates these effects using the parameters $A_{\text{ellipsoidal}}$, A_{beaming}, and $A_{\text{atmospheric}}$, which define the amplitudes of each component. To test the impact of the baseline variability on modelling outcomes, we carried out additional modeling using light curve data from which the between-eclipse modulation had been removed with a Savitzky–Golay filter, (referred to hereafter as 'flat-LC' data).

Initial modelling of the TIC 48227288 system revealed significant structure in the RV residuals. To address this, we modelled the RV baseline red noise using a Gaussian process (GP) with a real kernel and broad uniform priors on both the amplitude and timescale parameters (see Table B1). For TIC 339607421, the RV baseline was modelled using a simple offset, again with wide uniform priors (Table B2).

The joint posterior distributions were sampled using the ALLESFITTER dynamic, random walk nested sampling (NS) option, employing the DYNESTY package (Speagle 2020) with a set of 500 live points in the parameter space to explore the posterior distribution. The NS fits were run until a convergence threshold of $\Delta \ln Z \leq 0.01$ was reached, (where Z represents the Bayesian evidence determined during each iteration).

3.2.1 TIC 48227288: ALLESFITTER joint analysis results

The results of the joint analysis performed for the TIC 48227288 system are listed in Tables 5 and B1. Comparison of the original model results using the unfiltered light curve data with flat-LC model outcomes reveals only minor differences that, for the most part, fall within the stated parameter uncertainties. More significant discrepancies among the principal parameters are limited to the orbital period, surface brightness and secondary eclipse depth where differences are nonetheless small, ($\Delta P = 0.03$ s, $\Delta J_B = 0.004$ and $\Delta \delta_{\text{occ:TESS}} = 0.4$ ppt). This suggests that the baseline flux modulation was well captured in the original modeling. We therefore adopt the original model findings as our preferred ALLESFITTER modeling

solution for the TIC 48227288 system. Fits of this model to the RV and photometric data are shown in Figs 7 and 8.

The companion TIC 48227288B was found to have a radius of $0.605 \pm 0.011 \, R_\odot$ and mass $0.635 \pm 0.037 \, M_\odot$ consistent with a late K-class star and follows a short period, essentially circular orbit (a = 0.0492 ± 0.0009 au, P = 2.8963969 ± 0.0000001 d, e = $0.0013^{+0.0011}_{-0.0003}$). The orbital inclination is well constrained at $84.08^{+0.06}_{-0.05}°$. Both primary and secondary eclipses are well fit by the global model (Fig. 8, bottom panels) with depths of 134.4 ± 0.1 and 18.6 ± 0.1 ppt, respectively. The system geometry is such that the eclipses are nearly total, with approximately 96 per cent of the companion disc occluded during the secondary eclipse. While the baseline flux shows considerable modulation between eclipses, (Fig. 8, top panel), the inclusion of ellipsoidal variation, Doppler beaming, and atmospheric modulation terms appears to have adequately accounted for this.

The principal aim of this study is to constrain the stellar obliquity of the primary star. The large RV semi-amplitude exhibited by the TIC 48227288 system, ($K_B = 58.62^{+0.13}_{-0.14}$ km s^{-1}), renders the RM effect difficult to discern in Fig. 7. However, the RM perturbation is clearly evident after removing the orbital RV component and isolating the eclipse event, (Fig. 9). Its slight asymmetry suggests a low but non-zero obliquity, which is supported by the findings of the global model which indicates that TIC 48227288B follows a marginally misaligned, prograde orbit with a sky projected obliquity of $-17.8^{+1.9}_{-2.0}°$.

3.2.2 TIC 339607421: ALLESFITTER joint analysis results

The results of the ALLESFITTER joint analysis performed for the TIC 339607421 system are listed in Table 6 with additional results provided in Table B2. As is evident in Fig. 10, the variation in the TIC 339607421 light-curve baseline flux is notably more complex than that observed for TIC 48227288, with modulations occurring over a greater number of timescales. While efforts to fully model this baseline variation within the ALLESFITTER framework achieved only limited success, the modelling outcomes from both the original and flat-LC data sets are consistent within the stated uncertainties (see Table 6). Nevertheless, given the complications involved in modelling the between-eclipse baseline we adopt the flat-LC model as the preferred ALLESFITTER modelling solution for the TIC 339607421 system. Fits of the flat-LC model to the photometric and RV data are shown in Figs 11 and 12, respectively.

The companion TIC 339607421B has a radius $R_B = 0.291 \pm 0.006 \, R_\odot$ and mass $M_B = 0.294 \pm 0.013 \, M_\odot$) consistent with an M3–M4 class star. It follows an essentially circular orbit, (e = $0.0010^{+0.0011}_{-0.0004}$), with a period of $2.43821243 \pm 0.00000002$ d, a semi-major axis of 0.0391 ± 0.0008 au, and orbital inclination of $83.93 \pm 0.03°$. As expected for a smaller, cooler companion, the eclipse depths are more modest than in the TIC 48227288 system with primary and secondary eclipse depths of 56.66 ± 0.02 ppt and 3.98 ± 0.02 ppt, respectively. In contrast to TIC 48227288, the TIC 339607421 system experiences a full secondary eclipse, albeit briefly, with the companion completely occluded for $\sim$32 minutes during the secondary eclipse.

The RM effect was observed over three eclipses for this system. As can be seen in Fig. 13, the RM signature is less pronounced than in the TIC 48227288 system due to the smaller size of the companion, (the RM amplitude is approximately 600 m s^{-1} compared to 830 m s^{-1} for TIC 48227288). The RM perturbation is nearly symmetric, indicating a low stellar obliquity which is confirmed by the global
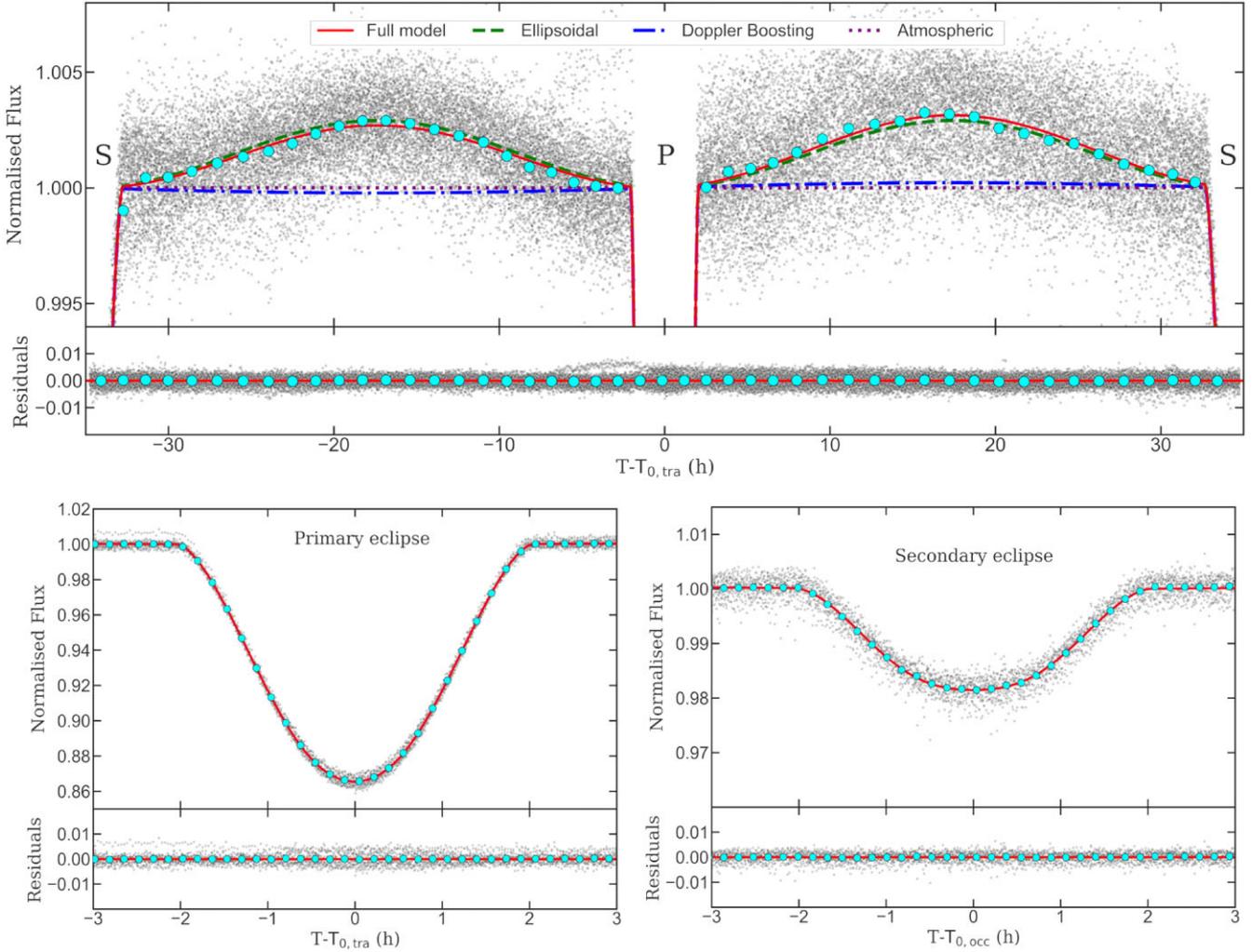
Figure 8. Phase folded TIC 48227288 *TESS* PDCSAP data showing the model fit to the flux baseline modulation (top), primary eclipse (bottom left) and secondary eclipse (bottom right). The positions of the primary and secondary eclipses in the top panel are marked by 'P' and 'S'. *TESS* observations are shown as gray points. Cyan circles are *TESS* observations binned with a cadence of 10 min (for both eclipses) and 90 min (out of eclipse data). Included in the phase curve model fit shown in the top graph are the ellipsoidal (green dashed line), atmospheric (purple dotted line) and beaming modulations(blue dash–dotted line). The combined median model fit is plotted as a solid red line in all plots. Residuals to the combined model are show in the bottom panels of each plot.

analysis which yields a sky projected obliquity, $\lambda = -14.7^{+5.4}_{-5.9}{}^{\circ}$. The combination of low median obliquity and larger associated uncertainties suggests that any misalignment in the TIC 339607421 system is likely to be minor.

### 3.3 Reloaded Rossiter–McLaughlin analysis

The classical RV based approach to measuring stellar obliquities, such as employed above, relies on modelling perturbations in the CCF centroid location caused by distortions that occur in the stellar lines during eclipse events. However, as noted by Cegla et al. (2016) and Bourrier et al. (2017, 2022), this method can introduce biases if the occulted portion of the stellar line profile is not accurately represented. In response to these limitations, the recently developed RRM technique offers an alternative approach that addresses some of the shortcomings of the more traditional analysis. The RRM method involves extracting the radial velocity ('local RV') of the stellar surface region occulted by the transiting companion. Using the framework of Cegla et al. (2016), it is then possible to use the local RVs to reconstruct the trajectory of the companion's 'shadow'

as it traverses the stellar disk, and thereby in turn determine the stellar obliquity.

To independently verify the obliquity estimates obtained from our ALLESFITTER analysis, we applied the RRM technique to a number of selected Minerva eclipse events (see Table 7). Each selected event includes a minimum of four high cadence observations taken either immediately prior to ingress, or shortly following egress.
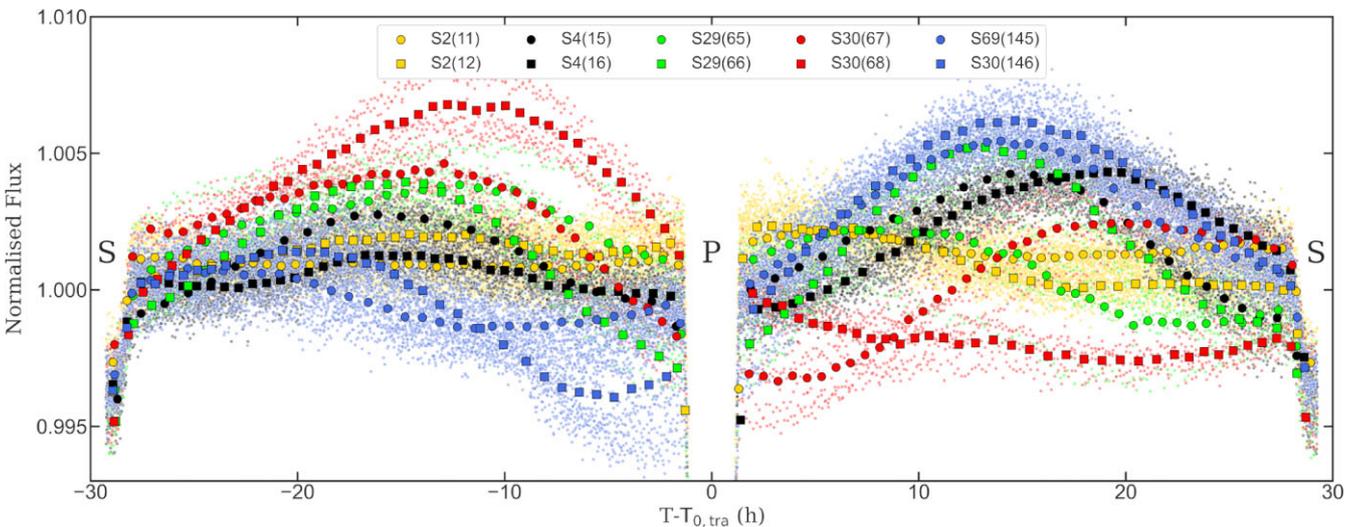
The RRM calculation then proceeded as follows. Disc-integrated CCFs generated during the computation of eclipse event RVs were first scaled by their median continuum flux level, (defined here as the CCF region $> 2\sigma$ from the computed RV, where σ is the Gaussian width of the CCF profile), and CCF uncertainties calculated from the standard deviation of the continuum region. ALLESFITTER light-curve and RV model predictions were then used to normalize the CCF's to account for loss of light during the eclipse and correct for Keplerian motion.

A master out-of-transit CCF for each eclipse event was then constructed by averaging all out-of-transit CCFs for that event. A Gaussian profile was fitted to each master CCF and the centroid RV determined and subsequently used to shift all CCFs for that event
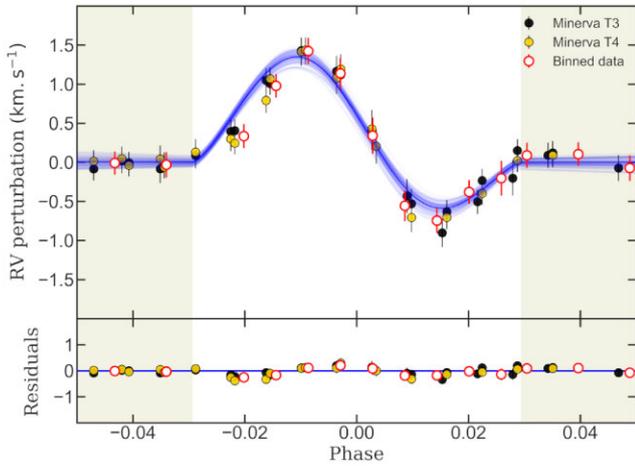
Figure 9. Phase folded radial velocity model of the Rossiter–McLaughlin effect for TIC 48227288 formed after subtraction of the orbital radial velocities. Observations from the two MINERVA telescopes used during eclipse events are shown as well as binned data to guide the eye. The white area marks the eclipse window. Blue lines show 100 randomly drawn posterior radial velocity models. Residual velocities to the best fit model are shown in the bottom panel.

into the stellar rest frame. Residual line profiles, representing the missing light from the stellar surface blocked by the companion, were then derived by subtracting each in-transit CCF from the corresponding master CCF. As an example, Fig. 14 presents the residual profiles generated for the TIC 48227288 transit 2a eclipse event. The corresponding trace plot, shown in the bottom panel of the figure, clearly shows the trajectory of the companion 'shadow' as it crosses the stellar disc. Following standard practice in RRM analyses (e.g. Allart et al. 2020; Bourrier et al. 2020), we excluded data points near the stellar limb, where reduced flux and lower signal-to-noise ratios (SNRs) due to partial occultation degraded the reliability of the extracted local RVs.

The remaining in-transit residuals were fitted with Gaussian functions to determine the local RVs. These measurements were then combined across all eclipse events for each system and modelled using the semi-analytic formalism of Cegla et al. (2016), initially assuming rigid-body stellar rotation. In this model, local RV values depend on the following: the orbital phase (ϕ), the scaled semi-major axis (a/R_A), orbital inclination (i_{orb}), radius of the secondary (R_B), sky-projected obliquity (λ), equatorial rotational velocity of the host star (v_A), and limb darkening (modelled using a quadratic law). Importantly, the stellar inclination, $i_\star$, is fixed at 90° and as such we are unable to determine the true obliquity, ψ_A and the value of v_A obtained in the model outcomes corresponds to $v_A \sin i$.
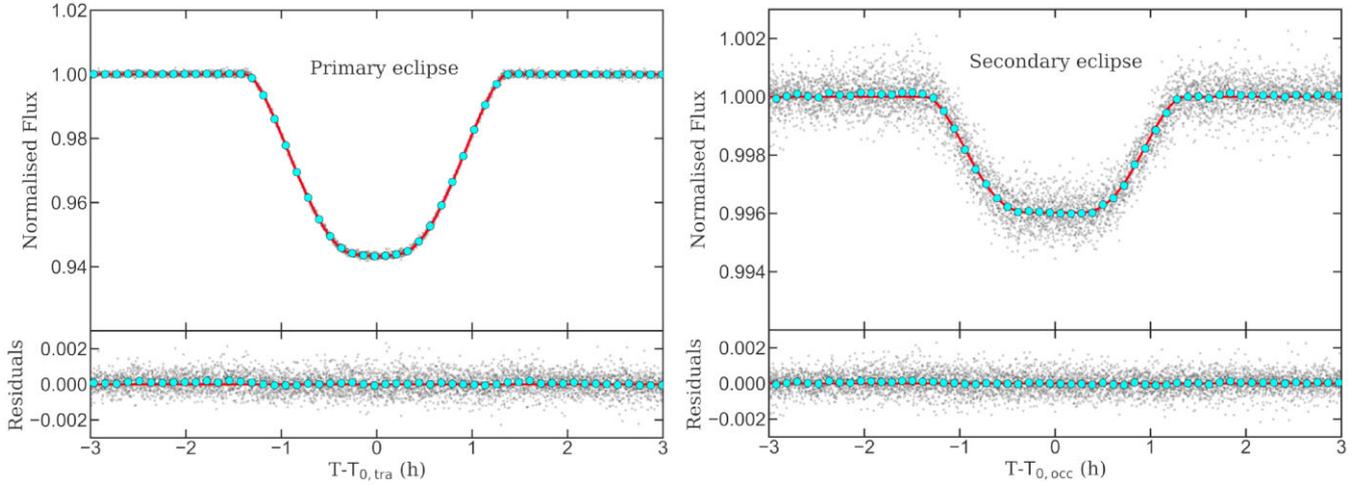
We employed the emcee MCMC sampler (Foreman-Mackey et al. 2013) to estimate the posterior distributions of the model parameters. Gaussian priors for (a/R_A, R_B, i_{orb}) as well as the quadratic limb darkening coefficients, U_1 and U_2 were informed by the ALLESFITTER posteriors derived in Section 3.2 while broad uniform priors were assigned to λ and v_A (see Table 8). Sampling utilized 50 walkers and continued until the number of steps exceeded ∼50 times the autocorrelation length. Final posterior distributions were computed after discarding an appropriate number of burn-in steps, which were determined visually.

We also explored an alternative model whereby rotation of the primary was allowed to vary with latitude (differential rotation model). In this framework, we independently sampled the equatorial rotational velocity, v_A, the stellar inclination $i_\star$, and the relative shear parameter α, where $\Omega = \Omega_{\mathrm{eq}}(1 - \alpha sin^2\theta)$), which describes the relative rotation rate between the poles and equator. Again, wide uniform priors were adopted (Table 8). By sampling $i_\star$ independently, we could compute the true three-dimensional obliquity (ψ) via:

$$\psi = \cos\left(\sin i_\star \cos \lambda \sin i_p + \cos i_\star \cos i_p\right)^{-1} \quad (1)$$

3.3.1 Reloaded Rossiter–McLaughlin results

The results of the RRM analysis for TIC 48227288 and TIC 339607421 are presented in Table 8 and the rigid model fits to the local RVs are shown in Fig. 15. From the rigid model we derive

Figure 10. Phase folded TIC 339607421 *TESS* PDCSAP data showing the variability in the baseline behavior between eclipses. The positions of the primary and secondary eclipses are marked by 'P' and 'S'. *TESS* observations are shown as smaller points colour coded with respect to the observation sector. Larger points show data binned to a cadence of ∼60 min. Binned data have been grouped not only by sector number but also orbit number (shown in brackets in the legend). The complex behaviour of the baseline over multiple timescales is clearly evident.

Figure 11. ALLESFITTER model fit to phase folded TIC 339607421 *TESS* PDCSAP data that has been filtered to remove baseline modulation. Left: Model fit to the primary eclipse. Right: Model fit to the secondary eclipse. *TESS* observations are shown as gray points. Cyan circles are *TESS* observations binned with a cadence of ∼6 min. The best-fitting model fit is plotted as a solid red line. Residuals are show in the bottom panels of each plot.
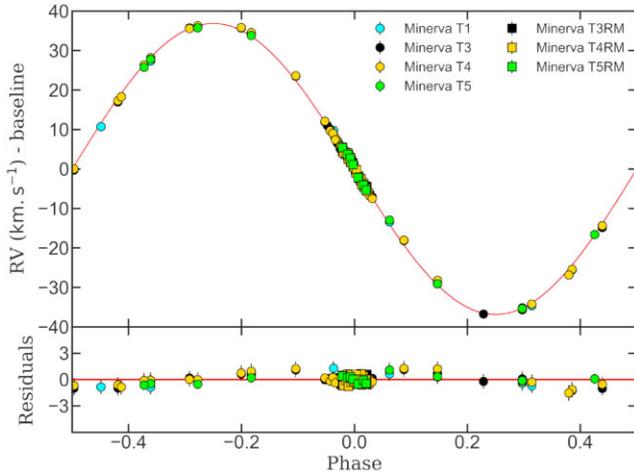
Figure 12. Phase folded radial velocity model for TIC 339607421 obtained from the ALLESFITTER analysis. Observations from each of the MINERVA telescopes are shown including observations made during the primary eclipse. The red line shown represents the best fit model. Residual velocities to the best fit model are shown in the bottom panel.

sky projected obliquities of $\lambda_A = -9.5 \pm 0.2°$ for TIC 48227288 and $\lambda_A = -8.2 \pm 0.2°$ for TIC 339607421. These values are lower than those obtained from the joint ALLESFITTER analyses ($-17.8°$ and $-14.7°$, respectively), but still indicate a minor level of misalignment in both systems, (as evidenced when we compare the position of the $\lambda = 0°$ model line with the best fit lines in Fig. 15). The values of $v_A \sin i_\star$ inferred from the rigid RRM model (17.9 ± 0.2 km s^{-1} for TIC 48227288 and 24.9 ± 0.2 km s^{-1} for TIC 339607421), were consistent within stated uncertainties with values determined from ISPEC analysis of MINERVA spectra and ALLESFITTER joint analysis of RV and photometric data (see Table 4).

When adopting a differential rotation model, (right-hand column of Table 8), we find sky projected obliquities of $\lambda_A = -10.5 \pm 0.2°$ for TIC 48227288 and $\lambda_A = -8.8 \pm 0.2°$ for TIC 339607421,
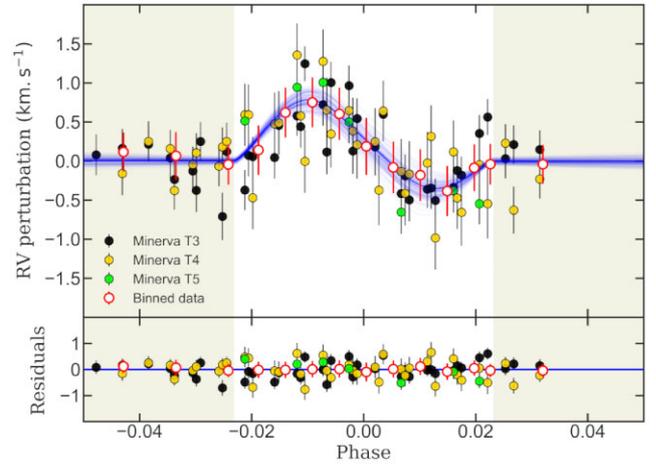
Figure 13. Phase folded radial velocity model of the Rossiter–McLaughlin effect for TIC 339607421 formed after subtraction of the orbital radial velocities. Observations from the three MINERVA telescopes used during eclipse events are shown as well as binned data to guide the eye. The white area marks the eclipse window. Blue lines show 100 randomly drawn posterior radial velocity models. Residual velocities to the best fit model are shown in the bottom panel.

Table 7. Details of MINERVA observations used in Reloaded RM modeling.

			Observations	
	Date	Telescope	Total	Out-of-eclipse
TIC 48227288				
Transit 1	Apr 1 2023	T3	16	6
Transit 2a	Apr 30 2023	T3	13	4
Transit 2b	Apr 30 2023	T4	14	4
TIC 339607421				
Transit 3a	Sept 9 2023	T3	19	9
Transit 3b	Sept 9 2023	T4	17	7
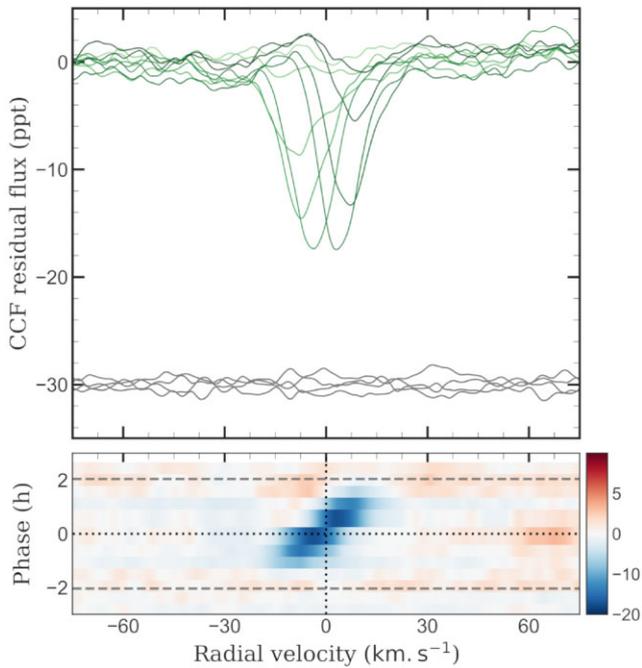
Figure 14. Upper panel: Residual line profiles extracted from MINERVA observations of the TIC 48227288 eclipse that took place on the night of 2023 April 30. Grey profiles are out-of-transit residuals that have been offset by 30 ppt to improve clarity. Lower panel: Trace plot illustrating the path of the Doppler shadow of the eclipsing body as it traverses the host star disc. Horizontal dashed lines show ingress and egress while the dotted line marks the mid eclipse point. The colour bar shows the CCF flux.

broadly consistent with the rigid model results. However, the inferred projected rotational velocities, ($v_A \sin i_\star = 12.2 \ \mathrm{km\,s^{-1}}$ and 20.3 $\mathrm{km\,s^{-1}}$ for TIC 48227288 and TIC 339607421, respectively), are significantly lower than indicated by the ISPEC, ALLESFITTER, or rigid body RRM modelling. Moreover, the differential rotation parameter, α, is poorly constrained and was constantly driven to the lower bounds of our uniform priors even when the lower bound was extended to the unrealistic value of -10. Due to these inconsistencies, we do not consider the differential rotation model results to be physically reliable and therefore disregard them in our subsequent analysis.

We note that the RRM technique has been predominantly applied to exoplanetary systems, and its application to binary star systems remains relatively unexplored (see Kunovac Hodžić et al. 2020). As such we were especially cognizant of the warning issued by Kunovac, that even in SB1 binaries such as those considered here, flux from the secondary component can potentially distort the cross-correlation function (CCF), thereby biasing the measurement of local RVs and yielding spurious misalignment signatures. For this to be a significant issue, however, the 'secondary' CCF generated during the analysis of the spectra must exceed the noise of the data and this is dependent not only on the light emitted by the secondary but also how the secondary spectra is impacted by convolution with the primary mask that is employed to generate the CCFs. As noted in Section 2.2 we used an F3V mask to generate TIC 48227288 CCFs and an F6V mask to generate TIC 339607421 CCFs. To assess the potential impact of the secondary component on our results, we visually inspected the out-of-transit CCFs generated using the aforementioned primary masks – paying particular attention to velocity regions where the secondary signal is expected based on the ALLESFITTER models. In all

cases, no secondary CCF was visually apparent suggesting that any contribution from the secondary component was likely suppressed below the general noise level, and thus did not significantly affect our analysis.

4 DISCUSSION

We report measurements of the sky-projected stellar obliquities for TIC 48227288 and TIC 339607421, contributing to the relatively limited sample of obliquity measurements available for binary stellar systems (Table A1). Sky projected obliquities were derived using both the classical radial velocity (RV) perturbation approach via the ALLESFITTER software package and also using the Reloaded Rossiter–McLaughlin (RRM) technique. The classical method yielded marginally misaligned prograde orbits for the companion stars ($\lambda_A = -17.8^{+1.9}_{-2.0}\,^\circ$ and $\lambda_A = -14.7^{+5.4}_{-5.9}\,^\circ$ for TIC 48227288 and TIC 339607421, respectively). The RRM analysis, assuming a rigidly rotating primary, returned smaller values ($\lambda_A = -9.5 \pm 0.2^\circ$ and $\lambda_A = -8.8 \pm 0.2^\circ$, respectively), yet still indicate slight misalignment.

According to pre-main-sequence (PMS) evolutionary models (e.g. Baraffe et al. 2015), both primary and secondary stars would have had significantly larger radii during their PMS phases. The current compact orbital configurations ($a/R_A \approx 6.6$ and 6.9 for TIC 48227288 and TIC 339607421, respectively) therefore suggest that the companions are unlikely to have formed in their current orbital positions, implying that a degree of orbital evolution has taken place. Potential mechanisms to drive that evolution include dynamical interactions with a third body, disc-driven migration, or perturbations from galactic tides. Analogous dynamical processes have been invoked for example by Mazeh & Shaham (1979) to explain close-in, misaligned hot Jupiter systems (such as observed for example by Addison et al. 2013, Dorval et al. 2020, and Cabot et al. 2021). In this respect, TIC 48227288 and TIC 339607421 make for valuable case studies, as the low companion masses, small mass ratios, and compact orbits, place TIC 48227288 and TIC 339607421 in the transitional parameter space between classical binaries and hot Jupiter systems (see Figs 16 to 18).

The present obliquities of these systems are shaped by both their dynamical histories and the effectiveness of tidal interactions in realigning the orbits. The strength of tidal interactions depends on the companion-to-host mass ratio, orbital separation, and the internal structure of the host star. Host stars on the main sequence with effective temperatures below the Kraft break, (here assumed to be $T_{\mathrm{eff,A}} = 6250\,\mathrm{K}$), have deeper convective envelopes that are more effective in dissipating the energy contained in tidal bulges generated by the nearby companion (Zahn 1977; Albrecht et al. 2012a). Because of this, convective host stars are thought to be more effective in realigning orbits than host stars operating above the Kraft break which possess radiative envelopes. Among exoplanet systems, this dependence manifests as broader obliquity distributions at longer scaled separations and lower mass ratios for convective hosts (Figs 17 and 18, top panels). These trends are not nearly so obvious in systems with radiative hosts (Figs 17 and 18, bottom panels), indicating that tidal alignment is less efficient. For binary stars, obliquity trends are less clear due to limited data, though most misaligned systems appear to involve primaries above the Kraft break (again see Figs 17 and 18).

System age is another key variable. Even in systems with modest tidal interaction, sufficient time can permit significant orbital realignment. To evaluate this, we adopt the tidal alignment timescale estimates from Albrecht et al. (2012b), (equations 2 and 3), and com-

Table 8. Median and 68 per cent confidence intervals for stellar parameters derived from the RRM analysis of TIC 48227288 and TIC 339607421 eclipse events. Priors are shown as uniform $\mathcal{U}(a,b)$ or normal $\mathcal{N}(\mu, \sigma)$. Notes:[†] preferred solution. [‡] fixed under rigid model assumption. * prior not used in rigid model. ** hard limits at 0,1 also imposed.

Parameter	Prior	Rigid body	Differential rotation
TIC 48227288			
Sky projected obliquity, λ_A (deg)	$\mathcal{U}(-180, 180)$	-9.5 ± 0.2 [†]	$-10.5 \pm +0.2$
Stellar rotational velocity, υ_A (km s^{-1})	$\mathcal{U}(0, 100)$	17.9 ± 0.2 [†]	13.3 ± 0.2
Stellar inclination, $i_\star$ (deg)	$\mathcal{U}(0, 180)$ *	90 [†] [‡]	$66.0^{+62.6}_{2.3}$
Differential rotation, α	$\mathcal{U}(-1, 1)$ *	0 [†] [‡]	$-0.99^{+0.02}_{-0.01}$
Orbital inclination, i_{orb} (deg)	$\mathcal{N}(84.08, 0.04)$	84.13 ± 0.06	84.14 ± 0.06
Semi-major axis to radius ratio, a/R_A	$\mathcal{N}(6.563, 0.030)$	$6.569^{+0.031}_{-0.029}$	6.572 ± 0.030
Companion Radius, R_B (R$_\odot$)	$\mathcal{N}(0.605, 0.011)$	$0.599 \pm +0.011$	$0.580^{+0.006}_{-0.008}$
LDC constant, U_1	$\mathcal{N}(0.16, 0.17)$**	$0.06^{+0.08}_{-0.04}$	$0.06^{+0.08}_{-0.05}$
LDC constant, U_2	$\mathcal{N}(0.39, 0.26)$**	$0.16^{+0.17}_{-0.11}$	$0.12^{+0.14}_{-0.09}$
True obliquity, ψ (deg)	....	....	28.9 ± 3.8
TIC 339607421			
Sky projected obliquity, λ_A (deg)	$\mathcal{U}(-180, 180)$	-8.2 ± 0.2 [†]	-8.8 ± 0.2
Stellar rotational velocity, υ_A (km s^{-1})	$\mathcal{U}(0, 100)$	24.9 ± 0.2 [†]	$21.2^{+1.9}_{-1.6}$
Stellar inclination, $i_\star$ (deg)	$\mathcal{U}(0, 180)$ *	90 [†] [‡]	$72.9^{+6.5}_{-6.1}$
Differential rotation, α	$\mathcal{U}(-1, 1)$ *	0 [†] [‡]	$-0.93^{+0.11}_{-0.06}$
Orbital inclination, i_{orb} (deg)	$\mathcal{N}(83.93, 0.03)$	83.93 ± 0.03	83.93 ± 0.03
Semi-major axis to radius ratio, a/R_A	$\mathcal{N}(6.932, 0.018)$	6.932 ± 0.018	6.932 ± 0.018
Companion Radius, R_B (R$_\odot$)	$\mathcal{N}(0.291, 0.006)$	0.291 ± 0.006	0.290 ± 0.006
LDC constant, U_1	$\mathcal{N}(0.30, 0.10)$**	0.35 ± 0.10	0.36 ± 0.10
LDC constant, U_2	$\mathcal{N}(0.02, 0.12)$**	$0.11^{+0.10}_{-0.08}$	$0.12^{+0.10}_{-0.08}$
True obliquity, ψ (deg)	....	....	$14.0^{+5.1}_{-4.0}$
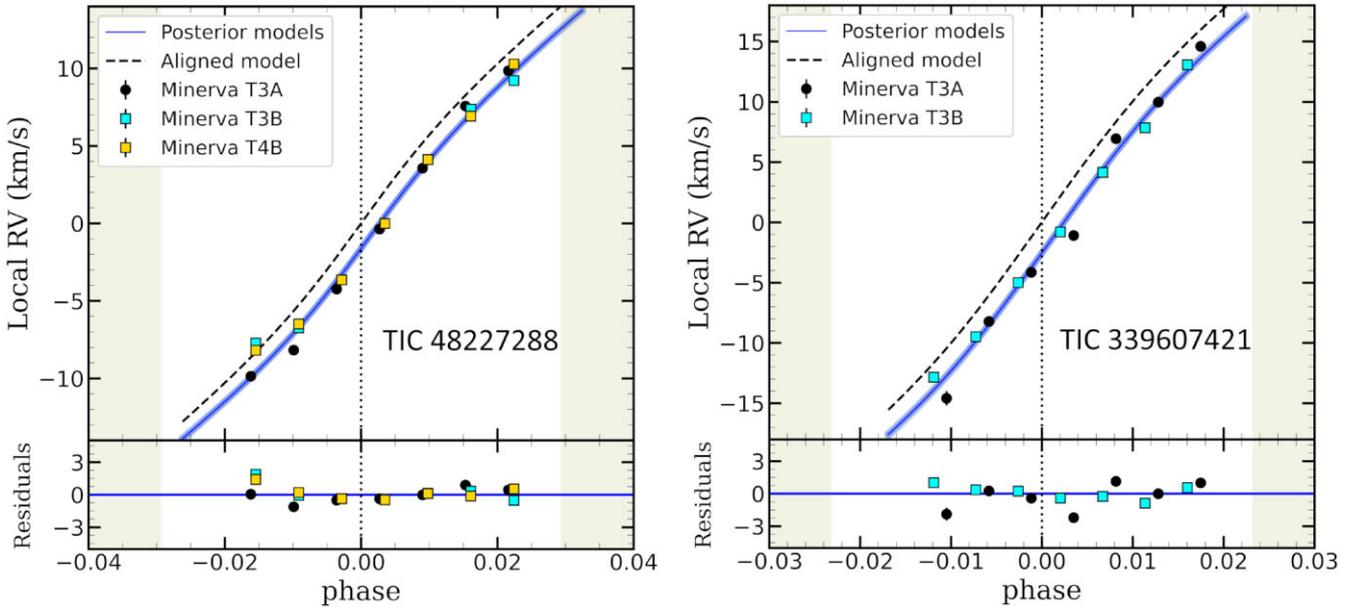
Figure 15. Reloaded RM fit to local radial velocities extracted for TIC 48227288 (left) and TIC 339607421 (right) assuming a rigidly rotating primary. Upper panels show the local RV as a function of phase for multiple eclipse observations accompanied by 50 randomly chosen Reloaded RM model posteriors. The dashed line marks the position of the best-fitting $\lambda = 0°$ model. Lower panels show the local velocity residuals against the best-fitting model. The eclipse window is shown as the white area while the vertical dotted line marks the mid eclipse time.
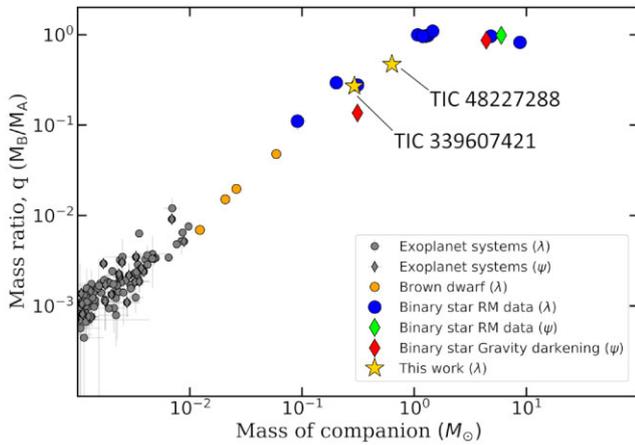
Figure 16. Log–log plot of the companion mass-mass ratio parameter space for published obliquity studies. In this and remaining obliquity graphs, exoplanetary obliquity studies are shown in grey, while brown dwarfs and binary star studies are colored. Sky projected obliquities, λ, and true obliquities, ψ, are designated by circles and diamonds, respectively. The two target systems that are the focus of this study are shown as yellow stars.

pare these to system ages (Fig. 19). These models include a number of simplifications but offer a relative measure of tidal effectiveness between different systems. Among exoplanets, higher misalignment correlates with lower age-to-alignment-time ratios, however this pattern is again less evident for binary star systems. For our two target systems, the ages are comparable to the estimated alignment timescale (age/alignment time ≈ 0.25 and 0.1 for TIC 48227288 and TIC 339607421, respectively), suggesting that alignment processes have had considerable time to act and so it is possible that the extent

of misalignment was historically greater that currently indicated by our modelling.

$$\frac{1}{\tau_{convective}} = \frac{1}{10 \times 10^9 \, yr} q^2 \left(\frac{a/R_\star}{40}\right)^{-6} \tag{2}$$

$$\frac{1}{\tau_{radiative}} = \frac{1}{0.25 \times 5 \times 10^9 \, yr} q^2 (1+q)^{5/6} \left(\frac{a/R_\star}{6}\right)^{-17/2} \tag{3}$$

Mechanisms such as Kozai–Lidov cycles (Kozai 1962), which can induce spin–orbit misalignment, also excite orbital eccentricity. Indeed, many binaries with measured obliquities exhibit significant eccentricities (Table A1; Fig. 20). However, both TIC 48227288B and TIC 339607421B follow circular orbits (e ≈ 0.001 in each case). Tidal theory predicts that orbital alignment proceeds more rapidly than orbital circularization in such systems, since orbital angular momentum far exceeds stellar spin angular momentum (Albrecht et al. 2014; Anderson, Lai & Storch 2017; Lin & Ogilvie 2017). Consequently, observing misalignment in a circular orbit, even a minor level of misalignment such as suggested by our modelling of the TIC 48227288 and TIC 339607421 systems, presents a theoretical challenge, as previously noted for the similar case of CV Velorum (Albrecht et al. 2014; e = 0, $\psi_A = 67°$). One explanation is ongoing dynamical perturbation by an unseen tertiary companion. As noted in Albrecht et al. (2014) this may indicate the continuing interaction with a third body that is producing spin–orbit misalignment despite the tidal damping taking place or, as pointed out by Justesen & Albrecht (2021), may hint at a more complicated formation migration history not well described by the current tidal theory.

Although not the primary objective of this study, our characterization of the low-mass companions in our target binary systems contributes useful data with which to test the accuracy of low-mass stellar evolutionary models. Previous studies of short-period, (P < 3 d), detached eclipsing binaries have reported that theoretical models systematically underestimate the radii of low-mass (M <
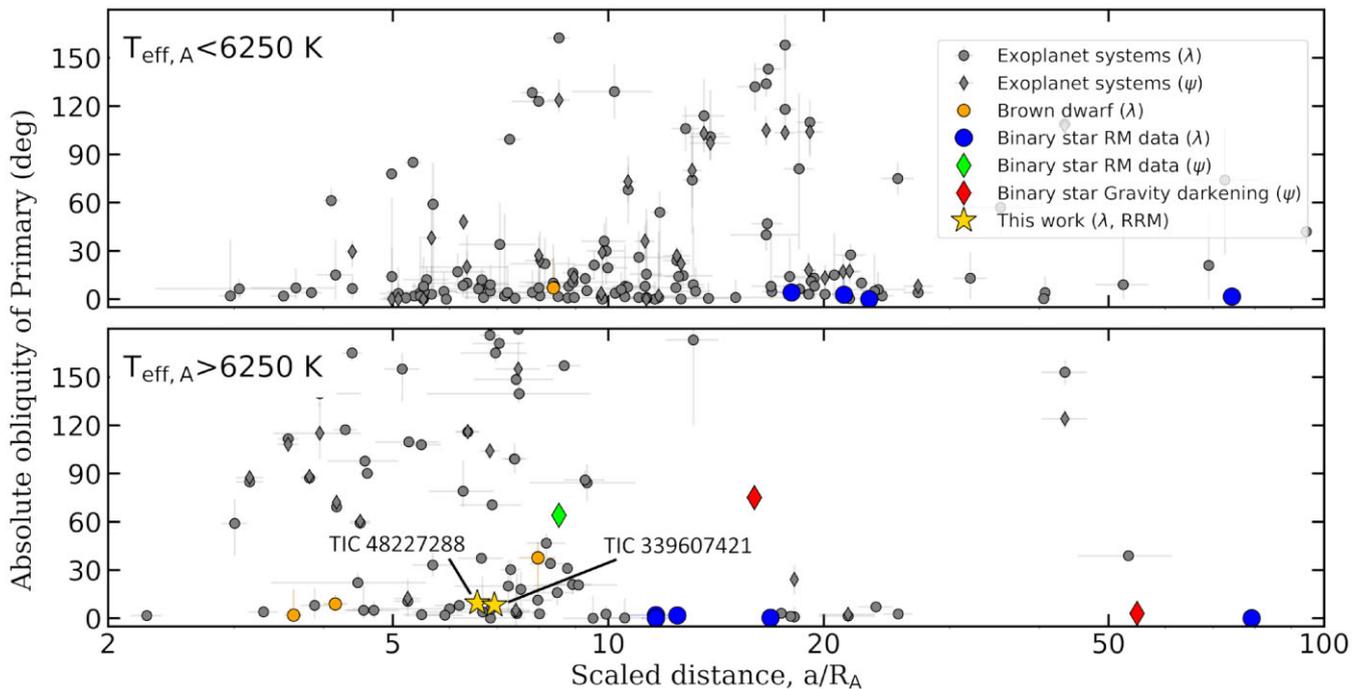
Figure 17. Absolute values of the projected, λ, and true obliquities, ψ, of exoplanetary, brown dwarf and binary star systems reported in the literature as a function of the scaled distance, a/R_A. Only primary star obliquities are shown for binary star systems. The two target systems that are the focus of this study and their corresponding RRM obliquities are shown as yellow stars.
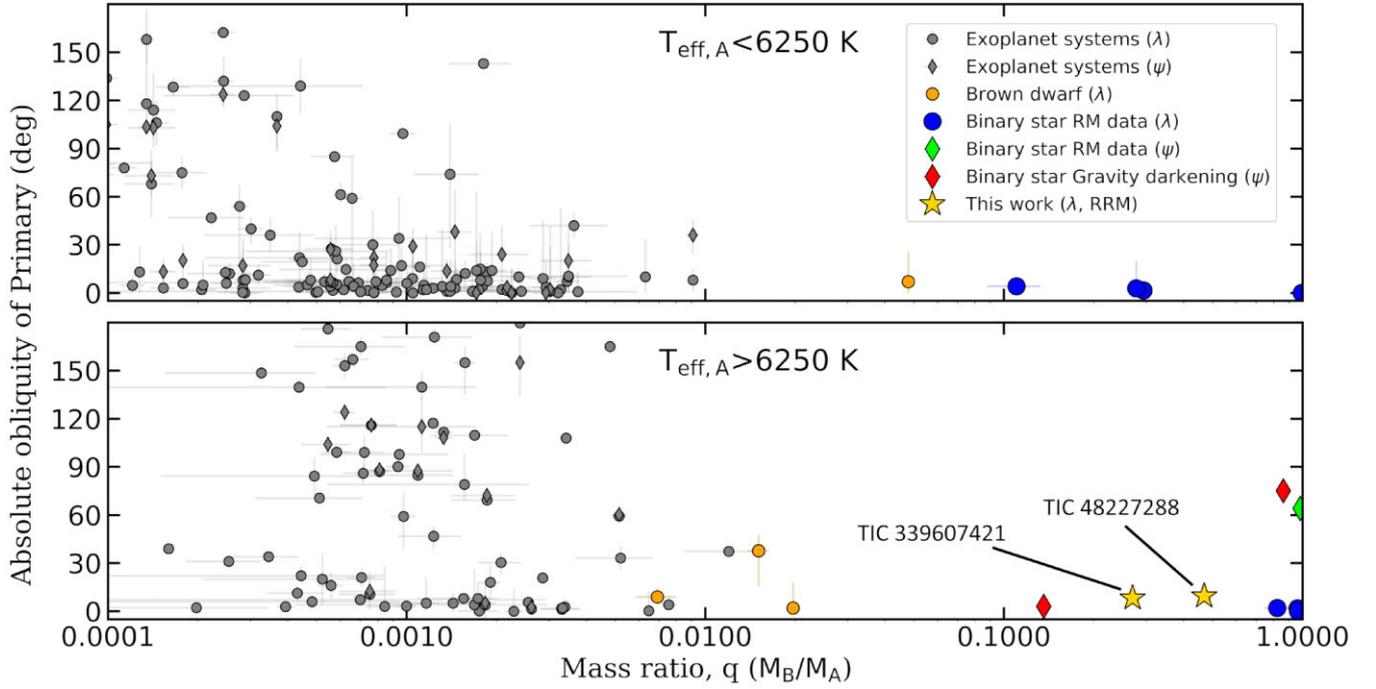
Figure 18. Absolute values of the projected, λ, and true obliquities, ψ, of exoplanetary and binary star systems reported in the literature as a function of the companion to host mass ratio, q. Only primary star obliquities are shown for binary star systems. The two target systems that are the focus of this study and their corresponding RRM obliquities are shown as yellow stars.
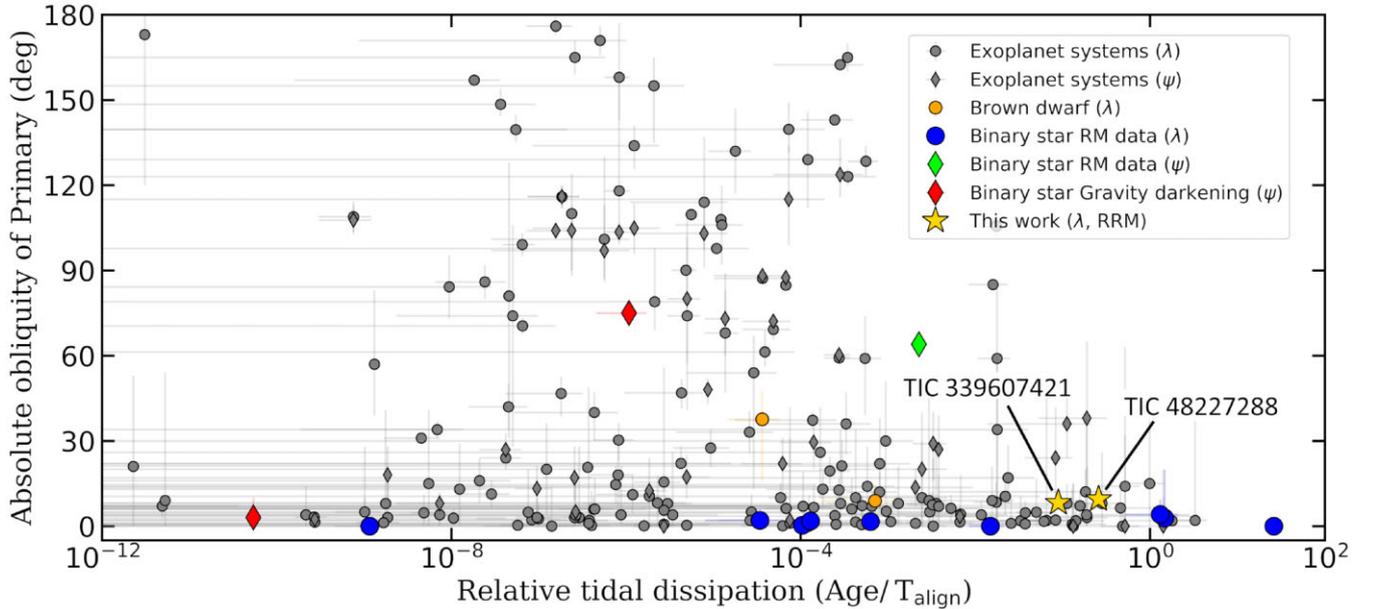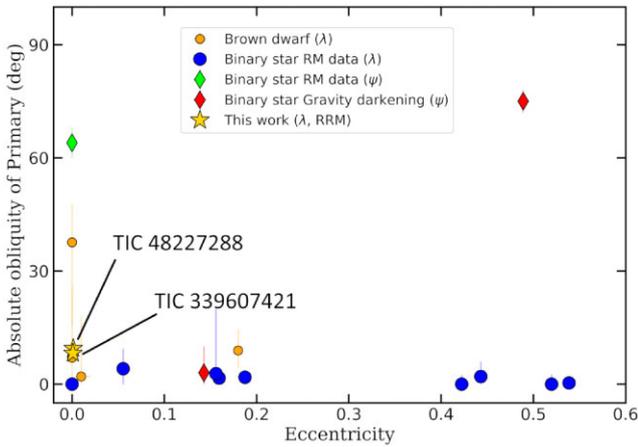

Figure 19. Absolute values of the projected, λ, and true obliquities, ψ, of exoplanetary and binary star systems as a function of their relative alignment time-scale. The two target systems that are the focus of this study and their corresponding RRM obliquities are shown as yellow stars.

$0.7\,M_\odot$) stars by as much as 5–20 per cent, with the discrepancy more pronounced for companion stars (Garrido et al. 2019; Cruz et al. 2022). TIC 48227288B and TIC 339607421B both lie within this regime and with the modelling we undertook, we were able to achieve mass and radius estimates with <6 per cent and <2 per cent uncertainties, respectively for each companion. Fig. 21 compares the derived companion mass/radii with theoretical mass-

radius model predictions, (Baraffe et al. 2015), for ages of 2 and 5 Gyr which bracket the estimated ages of our systems. Contrary to previous findings, we found that the theoretical models performed well in predicting the mass/radius characteristics of our two companions with TIC 339607421B falling within the 2 and 5 Gyr model predictions and TIC 48227288B agreeing within stated uncertainties.

Figure 20. Absolute values of the projected, λ, and true obliquities, ψ, of binary star systems as a function of their orbital eccentricities. The two target systems that are the focus of this study and their corresponding RRM obliquities are shown as yellow stars.
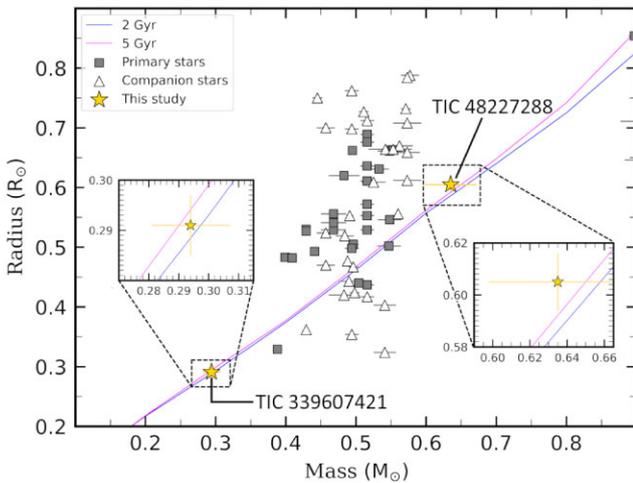
Figure 21. Stellar radius as a function of stellar mass. The plot compares observed mass/radius for low mass stars against theoretical predictions. Theoretical mass–radius models (Baraffe et al. 2015) for 2 and 5 Gyr models are shown as blue and red lines, respectively. The two low mass companions from this study are highlighted as yellow stars. Other data points are extracted from Garrido et al. (2019) and Cruz et al. (2022) where mass and radius uncertainties are <5 per cent.

5 CONCLUSIONS

In this study, we present an analysis of *TESS* photometric data and MINERVA radial velocity data to characterize two single-lined spectroscopic binary star (SB1) systems and estimate the obliquities of their primary stars.

TIC 339607421 comprises an F6V primary ($M_A = 1.09 \pm 0.04 \, M_\odot$, $R_A = 1.21^{+0.03}_{-0.02} \, R_\odot$) orbited by an M-dwarf companion ($M_B = 0.294 \pm +0.013 \, M_\odot$, $R_B = 0.291 \pm 0.006 \, R_\odot$) in a short period ($P_B \sim 2.4$ d), circular ($e \sim 0.001$) orbit. TIC 48227288 consists of an F3V primary ($M_A = 1.36^{0.06}_{-0.08} \, M_\odot$, $R_A = 1.61 \pm 0.03 \, R_\odot$) orbited by a late K-class companion ($M_B = 0.635 \pm 0.037 \, M_\odot$, $R_B = 0.605 \pm 0.011 \, R_\odot$) in a similarly short-period ($P_B \sim 2.9$ d), near circular ($e \sim 0.001$) orbit.

Analysis of the anomalous RV perturbation using ALLESFITTER yielded marginally misaligned prograde orbits for both systems, (TIC 48227288: $\lambda_A = -17.8^{+1.9}_{-2.0}$°, TIC 339607421: $\lambda_A = -14.7^{+5.4}_{-5.9}$°). RRM analysis yielded slightly lower obliquities, (TIC 48227288: $\lambda_A = -9.5 \pm 0.2$° and TIC 339607421: $\lambda_A = -8.2 \pm 0.2$°) but confirmed the minor misalignment inferred from the classical RV analysis.

These results contribute to the limited sample of binary systems involving cool primaries with measured obliquities. Notably, TIC 339607421 and TIC 48227288 represent the shortest period systems within this sample. The detection of slight misalignment for companions in circular orbits, along with a similar findings for systems such as CV Vel, suggests that current models of binary formation and orbital evolution may be incomplete and that further investigation of similar systems are warranted to enable a better understanding of the formation and evolution of binary star systems.

DATA AVAILABILITY

The MINERVA radial velocity data and *TESS* photometric data underlying this article are available in full in the online supporting material. The *TESS* data used in this paper are also available via

NASA's Mikulski Archive for Space telescopes: https://mast.stsci.edu/portal/Mashup/Clients/Mast/Portal.html

REFERENCES

Addison B. C., Tinney C. G., Wright D. J., Bayliss D., Zhou G., Hartman J. D., Bakos G. Á., Schmidt B., 2013, ApJ, 774, L9
Addison B. C., Tinney C. G., Wright D. J., Bayliss D., 2016, ApJ, 823, 29
Addison B. et al., 2019, PASP, 131, 115003
Ahlers J. P., Seubert S. A., Barnes J. W., 2014, ApJ, 786, 131
Albrecht S., Reffert S., Snellen I., Quirrenbach A., Mitchell D. S., 2007, A&A, 474, 565
Albrecht S., Reffert S., Snellen I. A. G., Winn J. N., 2009, Nature, 461, 373
Albrecht S., Winn J. N., Carter J. A., Snellen I. A. G., de Mooij E. J. W., 2011, ApJ, 726, 68
Albrecht S., Winn J. N., Fabrycky D. C., Torres G., Setiawan J., 2012a, in Richards M. T., Hubeny I., eds, From Interacting Binaries to Exoplanets: Essential Modelling Tools. Vol. 282, Kluwer, Dordrecht, p. 397
Albrecht S. et al., 2012b, ApJ, 757, 18
Albrecht S., Setiawan J., Torres G., Fabrycky D. C., Winn J. N., 2013, ApJ, 767, 32
Albrecht S. et al., 2014, ApJ, 785, 83
Allart R. et al., 2020, A&A, 644, A155
Andersen J., Garcia J. M., Gimenez A., Nordstrom B., 1987, A&A, 174, 107
Anderson K. R., Lai D., Storch N. I., 2017, MNRAS, 467, 3066
Armitage P. J., Clarke C. J., 1997, MNRAS, 285, 540
Astropy Collaboration et al., 2022, ApJ, 935, 167
Bailer-Jones C. A. L., Rybizki J., Fouesneau M., Demleitner M., Andrae R., 2021, AJ, 161, 147
Bakış V., Budding E., Erdem A., Bakış H., Demircan O., Hadrava P., 2006, MNRAS, 370, 1935
Baraffe I., Homeier D., Allard F., Chabrier G., 2015, A&A, 577, A42
Bate M. R., Lodato G., Pringle J. E., 2010, MNRAS, 401, 1505
Blanco-Cuaresma S., 2019, MNRAS, 486, 2075
Blanco-Cuaresma S., Soubiran C., Jofré P., Heiter U., 2014, in Singh H. P., Prugniel P., Vauglin I., eds, Astronomical Society of India Conference Series, Proceedings of the International Workshop on Stellar Spectral Libraries, Vol 11, p.85,
Bourrier V., Cegla H. M., Lovis C., Wyttenbach A., 2017, A&A, 599, A33
Bourrier V. et al., 2020, A&A, 635, A205
Bourrier V. et al., 2021, A&A, 654, A152
Bourrier V. et al., 2022, A&A, 663, A160
Cabot S. H. C. et al., 2021, AJ, 162, 218
Cannon A. J., Pickering E. C., 1993, VizieR Online Data Catalog: Henry Draper Catalogue and Extension (Cannon + 1918–1924; ADC 1989), VizieR Online Data Catalog: III/135A. Originally published in: Harv. Ann. 91–100 (1918-1924)
Castelli F., Kurucz R. L., 2003, in Piskunov N., Weiss W. W., Gray D. F., eds, New Grids of ATLAS9 Model Atmospheres. Modelling of Stellar Atmospheres. Vol. 210, Astronomical Society of the Pacific, Sweden, p. A20
Cegla H. M., Lovis C., Bourrier V., Beeck B., Watson C. A., Pepe F., 2016, A&A, 588, A127
Clark J. T. et al., 2023, AJ, 165, 207
Cruz P., Aguilar J. F., Garrido H. E., Diaz M. P., Solano E., 2022, MNRAS, 515, 1416
Cutri R. M. et al., 2003, VizieR Online Data Catalog: 2MASS All-Sky Catalog of Point Sources (Cutri+ 2003), VizieR On-line Data Catalog: II/246. Originally published in: University of Massachusetts and Infrared Processing and Analysis Center, (IPAC/California Institute of Technology) (2003)
Cutri R. M. et al., 2021, VizieR Online Data Catalog: AllWISE Data Release (Cutri + 2013), VizieR On-line Data Catalog: II/328 Originally published in: IPAC/Caltech (2013)
Dorval P. et al., 2020, A&A, 635, A60
Doyle L. et al., 2023, MNRAS, 522, 4499
Duchêne G., Kraus A., 2013, ARA&A, 51, 269

Eastman J., Gaudi B. S., Agol E., 2013, PASP, 125, 83
Espinoza N., Jordán A., 2015, MNRAS, 450, 1879
Foreman-Mackey D., Hogg D. W., Lang D., Goodman J., 2013, PASP, 125, 306
Fulton B. J., Petigura E. A., Blunt S., Sinukoff E., 2018, PASP, 130, 044504
Gaia Collaboration et al., 2023, A&A, 674, A1
Garrido H. E., Cruz P., Diaz M. P., Aguilar J. F., 2019, MNRAS, 482, 5379
Ghez A. M., McCarthy D. W., Patience J. L., Beck T. L., 1997, ApJ, 481, 378
Goodricke J., 1783, Philos. T. R. Soc. Lond. Ser. I, 73, 474
Goodricke J., 1784, Philos. T. R. Soc. Lond. Ser. I, 74, 287
Günther M. N., Daylan T., 2019, Astrophysics Source Code Library, record ascl:1903.003
Günther M. N., Daylan T., 2021, ApJS, 254, 13
Hale A., 1994, AJ, 107, 306
Henden A. A., Levine S., Terrell D., Welch D. L., 2015, in American Astronomical Society Meeting Abstracts #225. p. 336.16
Herschel W., 1785, Philos. T. R. Soc. Lond. Ser. I, 75, 40
Herschel W., 1802, Philos. T. R. Soc. Lond. Ser. I, 92, 477
Herschel M., Watson D., 1782, Philos. T. R. Soc. Lond. Ser. I, 72, 112
Høg E. et al., 2000, A&A, 355, L27
Holmgren D. E., Hill G., Fisher W., Scarfe C. D., 1990, A&A, 231, 89
Hube D. P., Couch J. S., 1982, Ap&SS, 81, 357
Hunter J. D., 2007, Comput. Sci. Eng., 9, 90
Husser T. O., Wende-von Berg S., Dreizler S., Homeier D., Reiners A., Barman T., Hauschildt P. H., 2013, A&A, 553, A6
Justesen A. B., Albrecht S., 2020, A&A, 642, A212
Justesen A. B., Albrecht S., 2021, ApJ, 912, 123
Kharchenko N. V., 2001, Kinematika i Fizika Nebesnykh Tel, 17, 409
Kozai Y., 1962, AJ, 67, 591
Kunovac Hodžić V. et al., 2020, MNRAS, 497, 1627
Kunovac Hodžić V., Triaud A. H. M. J., Cegla H. M., Chaplin W. J., Davies G. R., 2021, MNRAS, 502, 2893
Kurucz R., 1993, ATLAS9 Stellar Atmosphere Programs and 2 km/s Grid. Robert Kurucz CD-ROM No.13. Smithsonian Astrophysical Observatory, Cambridge, MA
Kuruwita R. L., Haugbølle T., 2023, A&A, 674, A196
Lai D., Foucart F., Lin D. N. C., 2011, MNRAS, 412, 2790
Lázaro C., Arévalo M. J., Antonopoulou E., 2006, MNRAS, 368, 959
Liang Y., Winn J. N., Albrecht S. H., 2022, ApJ, 927, 114
Lightkurve Collaboration, 2018, Astrophysics Source Code Library, record ascl:1812.013
Lin Y., Ogilvie G. I., 2017, MNRAS, 468, 1387
Marcussen M. L., Albrecht S. H., 2022, ApJ, 933, 227
Marcussen M. L., Albrecht S. H., Winn J. N., Su Y., Lundkvist M. S., Schlaufman K. C., 2024, ApJ, 975, 149
Mathieu R. D., 1994, ARA&A, 32, 465
Mazeh T., Shaham J., 1979, A&A, 77, 145
McLaughlin D. B., 1924, ApJ, 60, 22
Michell J., 1767, Philos. T. R. Soc. Lond. Ser. I, 57, 234
Philippov A. A., Rafikov R. R., 2013, ApJ, 768, 112
Popper D. M., 1982, ApJ, 254, 203
Priyatikanto R., Kouwenhoven M. B. N., Arifyanto M. I., Wulandari H. R. T., Siregar S., 2016, MNRAS, 457, 1339
Rossiter R. A., 1924, ApJ, 60, 15
Schlafly E. F., Finkbeiner D. P., 2011, ApJ, 737, 103
Shporer A., 2017, PASP, 129, 072001
Simon M., 1995, Ap&SS, 223, 45
Smith C. L., Moe M., Kratter K. M., 2024, ApJ, 975, 153
Speagle J. S., 2020, MNRAS, 493, 3132
Stassun K. G. et al., 2019, AJ, 158, 138
Struve O., Elvey C. T., 1931, MNRAS, 91, 663
Sybilski P., Pawłaszek R. K., Sybilska A., Konacki M., Hełminiak K. G., Kozłowski S. K., Ratajczak M., 2018, MNRAS, 478, 1942
Tohline J. E., 2002, ARA&A, 40, 349
Tokovinin A., Moe M., 2020, MNRAS, 491, 5158
Triaud A. H. M. J., 2018, in Deeg H. J., Belmonte J. A., eds, Handbook of Exoplanets, Springer, Cham, Switzerland, p. 2
Triaud A. H. M. J. et al., 2013, A&A, 549, A18

Twigg L. W., 1979, Thesis, University of Florida, Gainsville
Vines J. I., Jenkins J. S., 2022, MNRAS, 513, 2719
Winn J. N. et al., 2011, ApJ, 741, L1
Winters J. G. et al., 2019, AJ, 157, 216
Wittenmyer R. A., Horner J., Carter B. D., Kane S. R., Plavchan P., Ciardi D., MINERVA-Australis consortium, 2018, in Short W. Cairns I., eds, Proceedings of the 17th Australian Space Research Conference held in Sydney, Australia 13–15 November 2017. p 155.
Worek T. F., 1996, PASP, 108, 962
Worek T. F., Zizka E. R., King M. W., Kiewiet de Jonge J. H., 1988, PASP, 100, 371
Zahn J. P., 1977, A&A, 57, 383
Zhou G., Huang C. X., 2013, ApJ, 776, L35
Zhou G. et al., 2016a, AJ, 152, 136
Zhou G., Latham D. W., Bieryla A., Beatty T. G., Buchhave L. A., Esquerdo G. A., Berlind P., Calkins M. L., 2016b, MNRAS, 460, 3376
Zhou G. et al., 2017, AJ, 153, 211

SUPPORTING INFORMATION

Supplementary data are available at *MNRAS* online.

Table 2. TIC 48227288 radial velocities determined from MINERVA observations.

Table 3. TIC 339607421 radial velocities determined from MINERVA observations.

Figure 1. TIC 48227288 *TESS* PDCSAP light curves.

Figure 2. TIC 339607421 *TESS* PDCSAP light curves.

Please note: Oxford University Press is not responsible for the content or functionality of any supporting materials supplied by the authors. Any queries (other than missing material) should be directed to the corresponding author for the article.

APPENDIX A: PREVIOUS STUDIES

Table A1. Previous obliquity studies involving Binary star systems.

System	Spectral type	Period (d)	R_A, R_B ($R_\odot$)	Ecc.	λ_A	λ_B	ψ_A	ψ_B	Method[†]	Reference[‡]
β Lyrae	Be + B6-8II	12.9	6.0,15.2	<0.01	aligned?				1	1
V1010 Oph	A7IV-V +	0.7	2.0,1.3	0.072	aligned?				1	2
W Umi	A3V + G9IV	1.7	3.6,3.1	≡ 0	aligned?				1	3
δ Lib	A0V + K0IV	2.3	4.1,4.2	0.069	aligned?				1	4
V505 Sgr (a)	A2V + GIV	1.2	2.1,2.4	≡ 0	aligned?				1	5
V505 Sgr (b)	A2V + GIV	1.2	2.1,2.4	≡ 0	aligned?				1	6
AI Dra	A0V + F9.5V	1.2	2.1,2.4	≡ 0	aligned?				1	5
X Tri	A3V + G3IV	1.0	1.7,2.0	≡ 0	aligned?				1	3
RZ Cas	A3V + KIV	1.2	1.6,1.9	≡ 0	aligned?				1	3
U Sge	B8.5V + G3III	3.4	4.0,5.9	0.04	aligned?				1	3
WW Cyg	B8V + G4III	3.3	4.2,5.7	≡ 0	aligned?				1	3
Y Leo	A3V + K3IV	1.7	1.9,2.5	≡ 0	aligned?				1	3
RX Hya	A8 + K0IV	2.3	1.8,2.6	≡ 0	aligned?				1	3
β Per (a)	B8 + K2IV	2.9	2.7,3.5	≡ 0	aligned?				1	7
β Per (b)	B8 + K2IV	2.9	2.7,3.5	≡ 0	aligned?				1	8
RW Gem	B5-B6V + F0III	2.9	3.4,4.5	≡ 0	aligned?				1	3
Y Psc	A3V + K2IV	3.8	2.7,3.7	0.12	aligned?				1	3
TV Cas	A2V + G1IV	1.8	3.2,3.3	≡ 0	aligned?				1	3
ST Per	A3V + KIV	2.6	2.3,3.0	≡ 0	aligned?				1	3
U Cep	B7V + G8III	2.5	2.8,5.2	≡ 0	aligned?				1	3
TX Uma	B8V + F7-F8III	3.1	2.7,4.1	≡ 0	aligned?				1	3
W Del	A0-B9.5V + K0IV	4.8	2.4,4.6	0.2	aligned?				1	3
DE Dra	B0V + B2V	5.3	2.9,1.1	0.02	misaligned?				1	9
SW Cyg	A2V + K1IV	4.6	2.6,4.3	0.3	aligned?				1	3
RY Per	B4V + F0III	6.9	4.1,8.1	0.21	aligned?				1	3
RZ Sct	B2II + A0II-III	15.2	15.8,15.9	≡ 0	aligned?				1	3
AQ Peg	A2V + K1IV	5.6	2.7,4.8	0.24	aligned?				1	3
RY Gem	A2V + K0III-K1IV	9.3	2.4,6.2	0.16	aligned?				1	3
V1143 Cyg (a)	F5V + F5V	7.6	1.3,1.3	0.54	aligned?				1	10
DI Her (a)	B5V + B5V	10.6	2.7,2.5	0.49	aligned?				1	11
NY Ceph (a)	B0V + B2V	15.3	6.0,5.8	0.44	aligned?				1	12
NY Ceph (b)	B0V + B2V	15.3	6.0,5.8	0.44	-2.0 ± 4.0				2	13
DI Her (b)	B5V + B5V	10.6	2.7,2.5	0.49	-72.0 ± 4.0	84.0 ± 8.0			2	14
DI Her (c)	B5V + B5V	10.6	2.7,2.5	0.49	$-74.0^{+2.0}_{-3.0}$	$79.0^{+2.0}_{-3.0}$	75.0 ± 3.0	80.0 ± 3.0	3	15
V1143 Cyg (b)	F5V + F5V	7.6	1.3,1.3	0.54	-0.3 ± 1.5	1.2 ± 1.6			2	16
EP Cru (a)	B5V + B5V	11.1	3.6,3.5	0.19	1.8 ± 1.6	<17			2	17
EP Cru (b)	B5V + B5V	11.1	3.6,3.5	0.19			$6.0^{+7.1}_{-4.5}$		4	18
Kepler 16 (a)	K7 +	41.1	0.6,0.2	0.16	-1.6 ± 2.4	<18.3			2	19
Kepler 16 (b)	K7 +	41.1	0.6,0.2	0.16			$8.4^{+10.2}_{-5.2}$		4	18
KOI-368.01 (a)	A + M	110.3	2.3,0.2	0.14	$36.0^{+23.0}_{-17.0}$		$69.0^{+9.0}_{-10.0}$		3	20
KOI-368.01 (b)	A + M	110.3	2.3,0.2	0.14	10.0 ± 2.0		3.0 ± 7.0		3	21
KOI-368.01 (c)	A + M	110.3	2.3,0.2	0.14			$12.9^{+6.2}_{-4.8}$		4	18
AI Hya	F2m + F0V	8.3	3.9,2.8	0.23			$14.1^{+11.1}_{-7.4}$		4	18
Y Cyg	O9.5 IV + O9.5IV	3.0	5.8,5.8	0.15			$21.7^{+11.2}_{-12.2}$		4	18
QX car	B2V + B2V	4.5	4.3,4.1	0.28			$22.6^{+12.2}_{-12.0}$		4	18
V541 Cyg	B9.5 + B9.5	15.3	1.9,1.8	0.47			$15.9^{+21.7}_{-8.5}$		4	18
FM Leo (a)	F6V + F6V	6.7	1.8,1.2	0	0.0 ± 1.1	0.3 ± 27.4			5	22
FM Leo (b)	F6V + F6V	6.7	1.8,1.2	0			$8.1^{+36.2}_{-7.2}$		4	18
NN Del (a)	F8 +	99.3	1.6,2.2	0.52	0.0 ± 2.6				5	22
NN Del (b)	F8 +	99.3	1.6,2.2	0.52			$8.1^{+37.5}_{-5.6}$		4	18
V963 Cen (a)	G2V + G2V	15.3	1.4,1.4	0.42	0.0 ± 2.4				5	22
V963 Cen (b)	G2V + G2V	15.3	1.4,1.4	0.42			$8.1^{+37.5}_{-5.7}$		4	18
GG Lup	B7V + B9V	1.8	2.4,1.8	0.15			$30.4^{+17.6}_{-16.9}$		4	18
V364 Lac	A4m + A3m	7.4	3.3,3.0	0.29			$30.4^{+19.4}_{-17.9}$		4	18

Table A1 *– continued*

System	Spectral type	Period (d)	R_A, R_B ($R_\odot$)	Ecc.	λ_A	λ_B	ψ_A	ψ_B	Method[†]	Reference[‡]
					Sky projected and true obliquity, deg			
TOI 1338 (a)	F8 +	14.6	1.3,0.3	0.16	-2.8 ± 17.1				6	23
TOI 1338 (b)	F8 +	14.6	1.3,0.3	0.16			$25.6^{+26.3}_{-15.0}$		4	18
V530 Ori	G1V + M1V	6.1	1.0,0.6	0.09			$37.0^{+16.1}_{-18.8}$		4	18
V459 Cas	A1m + A1m	8.5	2.0,2.0	0.02			$32.5^{+19.8}_{-18.0}$		4	18
V578 Mon	B1V + B2V	2.4	5.4,4.3	0.08			$38.2^{+15.6}_{-19.6}$		4	18
PV Cas	B9.5V + B9.5V	1.8	2.3,2.3	0.03			$39.7^{+16.7}_{-20.2}$		4	18
V478 Cyg	09.5V + 09.5V	2.9	7.3,7.2	0.02			$41.5^{+17.5}_{-22.9}$		4	18
PT vel	A1V + A6V	1.8	2.1,1.6	0.13			$40.6^{+22.0}_{-22.5}$		4	18
V636 Cen	G0V + K2V	4.3	1.0,0.8	0.13			$46.4^{+20.0}_{-24.0}$		4	18
IQ Per	B8V + A6V	1.7	2.4,1.5	0.07			$44.2^{+23.0}_{-23.4}$		4	18
IT Cas	F3V + F3V	3.9	1.6,1.6	0.09			$43.3^{+24.4}_{-22.4}$		4	18
EK Cep	A1V + G5V	4.4	1.6,1.3	0.11			$46.7^{+22.4}_{-23.9}$		4	18
J1219?39b	K0V +	6.8	0.8,0.1	0.06	$-4.1^{+4.8}_{-5.3}$				5	24
CV Vel	B2.5V + B2.5V	6.9	4.1,4.0	0	52.0 ± 6.0	-3.7 ± 7.0	64.0 ± 4.0	46.0 ± 9.0	2	25
AS Cam	B8V + B9.5V	3.4	2.6,2.0	0.16			$87.9^{+2.1}_{-2.5}$		4	18
AI Phe	K0IV + F7V	24.6	2.9,1.8	0.19		-87.0 ± 17.0			5	22

Notes. [†] Methods: (1) RM effect–visual assessment from plot of RV perturbation; (2) RM effect–velocity profile modelling; (3) Gravity darkening; (4) Analysis of apsidal motion; (5) RM effect–broadening function (6) RM effect–reloaded RM.

[‡] References: (1) Rossiter (1924); (2) Worek et al. (1988); (3) Twigg (1979); (4) Bakış et al. (2006); (5) Worek (1996); (6) Lázaro, Arévalo & Antonopoulou (2006); (7) McLaughlin (1924); (8) Struve & Elvey (1931); (9)Hube & Couch (1982); (10) Andersen et al. (1987); (11) Popper (1982); (12) Holmgren et al. (1990); (13) Albrecht et al. (2011); (14) Albrecht et al. (2009); (15) Liang et al. (2022); (16) Albrecht et al. (2007); (17) Albrecht et al. (2013); (18) Marcussen & Albrecht (2022); (19) Winn et al. (2011); (20) Zhou & Huang (2013); (21) Ahlers et al. (2014); (22) Sybilski et al. (2018); (23) Kunovac Hodžić et al. (2020); (24) Triaud et al. (2013); (25) Albrecht et al. (2014).

APPENDIX B: ADDITIONAL FITTED AND DERIVED DATA

Table B1. Median and 68 per cent confidence intervals of additional astrophysical parameters derived for TIC 48227288 by ALLESFITTER. Priors are shown as uniform $\mathcal{U}$(a,b) or normal $\mathcal{N}(\mu, \sigma)$. Notes: [†] preferred solution.

Parameter	Prior	Best fit[†]	Best fit (flattened light curve)
Flux error scaling (ln relative flux)			
$\ln \sigma_{F,(120s)}$	$\mathcal{U}(-10.0, -3.0)$	-6.265 ± 0.003	-6.606 ± 0.003
Transformed limb darkening			
$q1_{TESS,A}$	$\mathcal{U}(0,1)$	$0.30^{+0.06}_{-0.09}$	$0.36^{+0.04}_{-0.05}$
$q2_{TESS,A}$	$\mathcal{U}(0,1)$	$0.15^{+0.21}_{-0.10}$	$0.09^{+0.07}_{-0.06}$
$q1_{TESS,B}$	$\mathcal{U}(0,1)$	$0.48^{+0.19}_{-0.14}$	$0.28^{+0.11}_{-0.07}$
$q2_{TESS,B}$	$\mathcal{U}(0,1)$	$0.64^{+0.22}_{-0.24}$	$0.77^{+0.16}_{-0.24}$
RV jitter (ln km s^{-1})			
$\ln \sigma_{jitter;T1(1800s)}$	$\mathcal{U}(-20, 3)$	$-8.09^{+6.29}_{-5.99}$	$-9.92^{+6.47}_{-6.19}$
$\ln \sigma_{jitter;T3(1500s)}$	$\mathcal{U}(-20, 3)$	$-9.81^{+4.48}_{-5.81}$	$-11.86^{+5.87}_{-5.30}$
$\ln \sigma_{jitter;T3RM(1500s)}$	$\mathcal{U}(-20, 3)$	$-5.94^{+4.15}_{-6.88}$	$-8.48^{+6.53}_{-7.08}$
$\ln \sigma_{jitter;T3(1800s)}$	$\mathcal{U}(-20, 3)$	$-8.05^{+5.26}_{-6.44}$	$-10.34^{+6.43}_{-5.95}$
$\ln \sigma_{jitter;T4RM(1500s)}$	$\mathcal{U}(-20, 3)$	$-13.33^{+5.83}_{-4.45}$	$-5.89^{+3.28}_{-4.12}$
$\ln \sigma_{jitter;T4(1500s)}$	$\mathcal{U}(-20, 3)$	$-7.97^{+3.92}_{-4.94}$	$-10.62^{+5.37}_{-5.95}$
$\ln \sigma_{jitter;T4(1800s)}$	$\mathcal{U}(-20, 3)$	$-7.28^{+4.76}_{-5.51}$	$-10.73^{+6.75}_{-6.06}$
$\ln \sigma_{jitter;T5(1500s)}$	$\mathcal{U}(-20, 3)$	$-5.92^{+5.07}_{-5.73}$	$-8.74^{+6.56}_{-6.32}$
RV baseline			
GP amplitude ln a; T1	$\mathcal{U}(-20, 20)$	$0.73^{+1.02}_{-0.84}$	$0.61^{+0.84}_{-0.67}$
GP time scale ln c; T1	$\mathcal{U}(-20, 20)$	$5.16^{+8.97}_{-7.43}$	$3.49^{+8.08}_{-6.10}$
GP amplitude ln a; T3	$\mathcal{U}(-20, 20)$	$0.55^{+0.47}_{-0.34}$	$0.57^{+0.47}_{-0.33}$
GP time scale ln c; T3	$\mathcal{U}(-20, 20)$	$-2.62^{+0.47}_{-0.60}$	$-2.44^{+0.52}_{-0.63}$
GP amplitude ln a; T3RM	$\mathcal{U}(-20, 20)$	$-4.09^{+1.02}_{-6.13}$	$-3.79^{+0.83}_{-2.76}$
GP time scale ln c; T3RM	$\mathcal{U}(-20, 20)$	$7.36^{+7.78}_{-8.42}$	$8.32^{+7.36}_{-5.84}$
GP amplitude ln a; T4	$\mathcal{U}(-20, 20)$	$0.85^{+0.58}_{-0.40}$	$0.77^{+0.50}_{-0.39}$
GP time scale ln c; T4	$\mathcal{U}(-20, 20)$	$-3.12^{+0.51}_{-0.64}$	$-3.08^{+0.49}_{-0.58}$
GP amplitude ln a; T4RM	$\mathcal{U}(-20, 20)$	$-10.40^{+5.14}_{-5.68}$	$-6.90^{+2.89}_{-5.23}$
GP time scale ln c; T4RM	$\mathcal{U}(-20, 20)$	$7.99^{+8.15}_{-11.77}$	$3.28^{+10.53}_{-14.44}$
GP amplitude ln a; T5	$\mathcal{U}(-20, 20)$	$1.86^{+1.83}_{-1.10}$	$1.77^{+1.74}_{-0.97}$
GP time scale ln c; T5	$\mathcal{U}(-20, 20)$	$-4.93^{+1.32}_{-2.32}$	$-4.84^{+1.28}_{-2.43}$

Table B2. Median and 68 per cent confidence intervals of additional astrophysical parameters derived for TIC 339607421 by ALLESFITTER. Priors are shown as uniform $\mathcal{U}$(a,b) or normal $\mathcal{N}(\mu, \sigma)$. Notes:[†] preferred solution.

Parameter	Prior	Best fit	Best fit (flattened light curve)[†]
Flux error scaling (ln relative flux)			
$\ln \sigma_{F,(120s)}$	$\mathcal{U}(-10.0, -3.0)$	-6.506 ± 0.003	-7.546 ± 0.003
$\ln \sigma_{F,(600s)}$	$\mathcal{U}(-10.0, -3.0)$	-5.818 ± 0.008	-7.987 ± 0.008
Transformed limb darkening			
$q1_{TESS,A}$	$\mathcal{U}(0,1)$	$0.16^{+0.04}_{-0.03}$	0.10 ± 0.01
$q2_{TESS,A}$	$\mathcal{U}(0,1)$	$0.36^{+0.27}_{-0.22}$	$0.47^{+0.15}_{-0.18}$
$q1_{TESS,B}$	$\mathcal{U}(0,1)$	$0.44^{+0.31}_{-0.27}$	$0.73^{+0.17}_{-0.18}$
$q2_{TESS,B}$	$\mathcal{U}(0,1)$	$0.41^{+0.33}_{-0.26}$	$0.56^{+0.22}_{-0.19}$
RV jitter (ln km s^{-1})			
$\ln \sigma_{\mathrm{jitter;T1(1800s)}}$	$\mathcal{U}(-20, 3)$	-0.19 ± 0.27	$-0.24^{+0.27}_{-0.25}$
$\ln \sigma_{\mathrm{jitter;T3RM(900s)}}$	$\mathcal{U}(-20, 3)$	$-6.06^{+4.41}_{-8.55}$	$-5.78^{+4.13}_{-8.18}$
$\ln \sigma_{\mathrm{jitter;T3(900s)}}$	$\mathcal{U}(-20, 3)$	$-10.28^{+5.56}_{-6.29}$	$-9.85^{+5.21}_{-6.06}$
$\ln \sigma_{\mathrm{jitter;T3(1800s)}}$	$\mathcal{U}(-20, 3)$	$-0.20^{+0.22}_{-0.20}$	$-0.25^{+0.22}_{-0.20}$
$\ln \sigma_{\mathrm{jitter;T4RM(900s)}}$	$\mathcal{U}(-20, 3)$	$-1.19^{+0.24}_{-0.28}$	$-1.19^{+0.25}_{-0.30}$
$\ln \sigma_{\mathrm{jitter;T4(900s)}}$	$\mathcal{U}(-20, 3)$	$-10.91^{+5.86}_{-5.82}$	$-11.52^{+6.10}_{-5.53}$
$\ln \sigma_{\mathrm{jitter;T4(1800s)}}$	$\mathcal{U}(-20, 3)$	$-0.13^{+0.19}_{-0.18}$	$-0.17^{+0.19}_{-0.17}$
$\ln \sigma_{\mathrm{jitter;T5RM(900s)}}$	$\mathcal{U}(-20, 3)$	$-10.07^{+7.06}_{-6.70}$	$-4.78^{+3.17}_{-5.27}$
$\ln \sigma_{\mathrm{jitter;T5(1800s)}}$	$\mathcal{U}(-20, 3)$	-0.58 ± 0.33	$-0.62^{+0.32}_{-0.33}$
RV offset (km s^{-1})			
$\Delta RV_{\mathrm{T1(1800s)}}$	$\mathcal{U}(6,26)$	$16.06^{+0.28}_{-0.29}$	16.09 ± 0.28
$\Delta RV_{\mathrm{T3RM(900s)}}$	$\mathcal{U}(6,26)$	16.24 ± 0.08	16.22 ± 0.09
$\Delta RV_{\mathrm{T3(900s)}}$	$\mathcal{U}(6,26)$	16.43 ± 0.07	16.39 ± 0.07
$\Delta RV_{\mathrm{T3(1800s)}}$	$\mathcal{U}(6,26)$	$15.83^{+0.23}_{-0.22}$	$15.83^{+0.21}_{-0.22}$
$\Delta RV_{\mathrm{T4RM(900s)}}$	$\mathcal{U}(6,26)$	15.94 ± 0.10	15.92 ± 0.10
$\Delta RV_{\mathrm{T4(900s)}}$	$\mathcal{U}(6,26)$	16.31 ± 0.07	16.29 ± 0.07
$\Delta RV_{\mathrm{T4(1800s)}}$	$\mathcal{U}(6,26)$	$15.75^{+0.20}_{-0.19}$	15.72 ± 0.20
$\Delta RV_{\mathrm{T5RM(900s)}}$	$\mathcal{U}(6,26)$	$16.02^{+0.11}_{-0.12}$	$16.00^{+0.12}_{-0.11}$
$\Delta RV_{\mathrm{T5(1800s)}}$	$\mathcal{U}(6,26)$	$15.92^{+0.21}_{-0.20}$	$15.92^{+0.20}_{-0.19}$

This paper has been typeset from a TEX/LATEX file prepared by the author.